SNOW AND ICE MELT CONTRIBUTIONS TO HIMALAYAN FLOODS

JAMES RISING, UPMANU LALL

Abstract. Snow and ice melt form significant contributions to river base flows throughout the Himalayas, but their contribution to seasonal and catastrophic flooding is unclear. As glaciers melt and winter accumulation and temperature patterns shift with climate change, this contribution will cause changes to flood risk. This paper applies a new physical model of streamflow to estimate the separate contributions of precipitation and melt to historical flows at the Bhakra Dam on the Sutlej river, in the Indus River Basin. At the Bhakra dam, 26% of the flow volume of historical floods within our dataset is attributable to melt. A multivariate copula-based probability model produces a similar result for the 10-year flood. Using the model parameters calibrated for the Bhakra inflow, we find that the contribution of melt to flood flows varies over the basin, being higher at high elevation and in smaller basins, and is between 10 to 30% for the larger Indus river basin. We also perform sensitivity checks across a range of increases in temperature and precipitation.

1. Introduction

Throughout the Himalayan river basins, flooding has become increasingly problematic over recent decades, and in many areas the magnitude and frequency of severe floods is expected to increase further with climate change (Mirza, 2003, Mirza et al., 2003). The role that glacier melt plays in flooding remains uncertain, but the general trend is clear: the IPCC warns that "glacier melt in the Himalayas is projected to increase flooding, and rock avalanches from destabilized slopes, and to affect water resources within the next two to three decades. This will be followed by decreased river flows as the glaciers recede" (Parry, 2007).

This research attempts to distinguish between the effects of snow and ice melt and of changing precipitation patterns on flood frequency. We focus on the catchment basin of the Bhakra dam on the Satluj River, a tributary of the Indus, in northern India.

A growing body of literature examines the implications that this glacier retreat will have on water availability (e.g., Xu et al., 2009, Dairaku et al., 2008) for the 50-60% of the world's population that relies on glacier runoff (Barnett et al., 2005). The upper Indus river has greater than 70% of its flow from snow and ice melt (Jeelani et al., 2012). How snow and ice melt affect flood dynamics is an open question.

Glaciers in the Himalayas have a wide variety of temperature profiles, ambient annual temperatures, and ablation characteristics (Huang, 1990). However, because of the monsoon regime, these glaciers share some peculiarities, including simultaneous accumulation and ablation in summer (Ageta, 1983), and the potential for more rapid retreat than glaciers in other regions of the world (Fujita, 2008). Kaser et al. (2003) finds that glaciers also buffer precipitation (smoothing precipitation peaks), so a decrease in glacier area, and not just resulting melt, might result in increased flooding.

Since the catastrophic Khumbu Himal flood in 1985, Glacial Lake Outburst Floods (GLOFs) have been an active topic for research (Kattelmann, 2003). Within 10 km of the GLOF source, discharge (streamflow) from the GLOF can reach 60 times the corresponding maximum seasonal high flow flood discharge, but it drops with distance (Desloges and Church, 1992, Cenderelli and Wohl, 2001). Typically, GLOF flood waves dissipate within 30 km of their source (Richardson and Reynolds, 2000). We do not address GLOFs, since the processes behind them are very different from normal melt flow.

Our approach uses a new physically based hydrological model (section 2). Using remote sensing and flow measurements, the model is calibrated to the Bhakra dam basin (section 3). We analyze the contribution of melt to historical floods to estimate the effects for 10-year and 100-year catastrophic floods (section 3).[1] Finally, we perform sensitivity analysis for climate change by considering a variety of simple weather adjustment scenarios (section 3).

2. Drainage Model

The physical drainage model used in this paper is an extension of the SNOWMOD model developed by Singh and Jain (2003), aimed at predicting streamflow magnitudes from observed input data (precipitation, temperature, and topography). The model addresses surface runoff, channel flow, and subsurface flow.

Unlike SNOWMOD, our model is gridded, and uses a network of streamflow paths based on high-resolution topography data. It uses a single set of parameters for the entire basin, rather than different parameters by sub-basin, so that an application can also be made to the larger Indus basin. It also keeps track of precipitation-derived and melt-derived flow volumes separately, while combining them for flow rate calculations.

The model uses dynamically determined time step sizes, satisfying the Courant condition, with typically less than 1 hour per time-step. Figure 1 displays a diagram of the model's logic, which is described in the equations below.

Runoff Equations. The model is informed by the following inputs:

(1) $P(t, x, y)$, the precipitation, in $\frac{mm}{day}$.

(2) $T(t, x, y)$, the temperature, in $^\circ C$.

(3) $S(t, x, y)$, the existence of snow or ice cover, as a portion of grid cell area.

(4) $\xi(x, y)$, the DEM elevation across the basin, used to derive D∞ flow directions and slopes.

The fitted parameters of the model are:

[1] A number of metrics could be used to describe the magnitude of a flood. Perhaps the most natural is area flooded, although this can be difficult to model even with a detailed topographical map. Human-oriented metrics, like the number of people people affected or displaced and the economic damages, do not correlate well with the underlying hydrological magnitudes. The most frequent measure is streamflow, in either cusecs or m^3/s, on the principle that a flood is essentially a river that is flowing too much. This paper will focus on this measure.

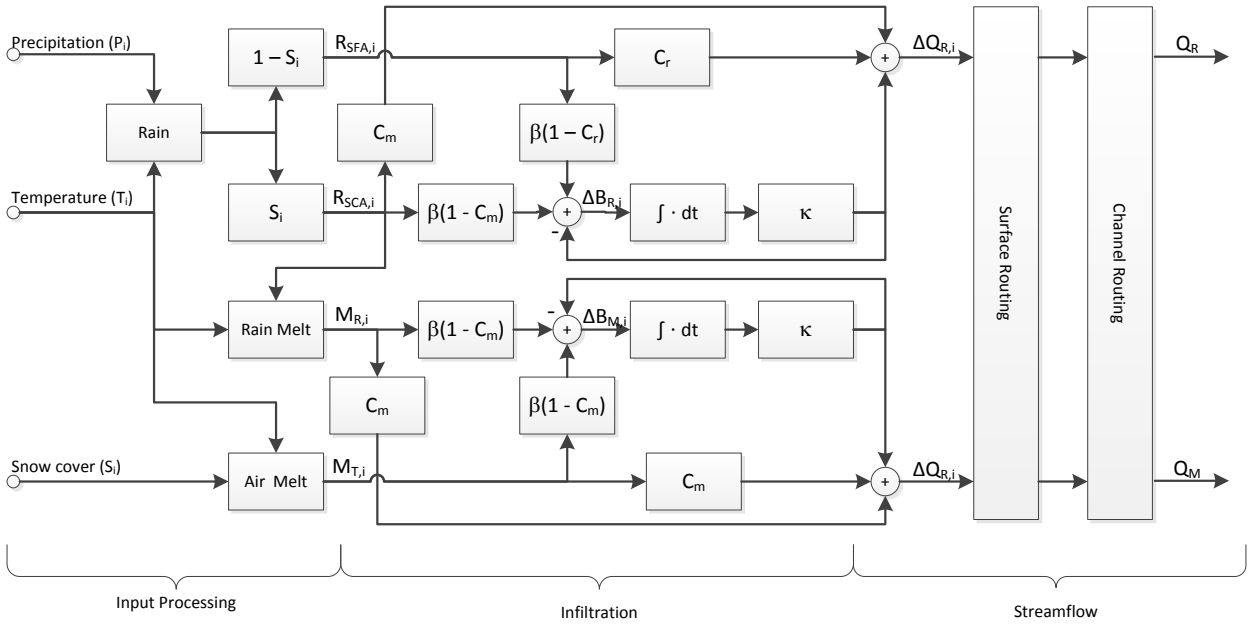

Figure 1: Schematic of the physical model, based on Singh and Jain (2003). Precipitation, temperature, and snow/ice cover result in rain runoff, melt runoff, and groundwater separately attributable to rain and melt. These flows are routed according to topographic paths calculated with TauDEM (Tarboton, 2005).

(1) $D(\xi(x,y))$, the degree day melt coefficient of snow/ice at a given level of elevation ($\xi(x,y)$), in $\frac{mm}{^\circ C day}$. The coefficients are used to determine snow and ice melt by a temperature-index method (see Ohmura, 2001), allowed to vary by elevation, as suggested by the results in Kayastha et al. (2003).

(2) C_r and C_m, the runoff coefficient for rain and melt, respectively.

(3) β, the portion of water entering the groundwater which asymptotically contributes to the base flow.

(4) κ, the portion of the existing groundwater which contributes to the baseflow each day.

Below, $\mathbf{1}\{\cdot\}$ is the indicator function, with a value of 1 where $\cdot$ is true, and 0 otherwise. The variables which vary in space and time will be denoted by the subscript i, where i varies over all space and time (e.g., $P_i = P(t_i, x_i, y_i)$).

Precipitation can fall as either rain or snow/ice, and the state is gauged using mean temperature (T_i), as in SNOWMOD. Rain contributes directly to runoff, while snowfall only contributes to runoff through melt in snow/ice-covered regions (as determined by the SSM/I maps). The portion of precipitation that falls as rain is estimated as,

$$R_i = \begin{cases} 0 & \text{if } T_i \leq 0^\circ C \\ P_i & \text{if } T_i > T_r = 2^\circ C \\ \frac{T_i}{T_r} P_i & \text{if } 0^\circ C < T_i \leq T_r \end{cases}$$

Rain that falls in regions covered by snow and ice is treated differently, so we define the rain on snow/ice-free areas ($R_{SFA,i}$) and rain on snow/ice-covered areas ($R_{SCA,i}$):

$$R_{SFA,i} = R_i(1 - S_i)$$
$$R_{SCA,i} = R_i S_i$$

Melt is determined from two sources. Rain on snow/ice produces melt (equation from Singh and Jain (2003)):

$$M_{R,i} = 4.2 T_i R_{SCA,i} \mathbf{1}\{T_i > 0°C\}/325$$

Snow/ice also melts as a linear response to temperature:

$$M_{T,i} = D_i S_i T_i \mathbf{1}\{T_i > 0°C\}$$

These components contribute to the streamflow through direct runoff and subsurface flow or baseflow. We handle rain and melt flow separately. For baseflow,

$$\Delta B_{R,i} = \beta\left((1 - C_r)R_{SFA,i} + (1 - C_m)R_{SCA,i}\right) - \kappa B_{R,i-1}$$
$$\Delta B_{M,i} = \beta(1 - C_m)\left(M_{R,i} + M_{T,i}\right) - \kappa B_{M,i-1}$$

where $\Delta B_{R,i}$ is the change in baseflow attributed to rain, and $\Delta B_{M,i}$ is the change in baseflow attributed to melt. $B_{\cdot,i-1}$ is corresponding baseflow from the previous day, of which $\kappa B_{\cdot,i-1}$ is released to the surface runoff.

Combined, the components of runoff are:

$$\Delta Q_{R,i} = C_r R_{SFA,i} + C_m R_{SCA,i} + \kappa B_{R,i-1}$$
$$\Delta Q_{M,i} = C_m\left(M_{R,i} + M_{T,i}\right) + \kappa B_{M,i-1}$$

These runoff components are then added to the existing runoff in each grid cell, and both the rain and melt flows are combined for calculations of flow velocity.

The parameters available for calibration are C_r, C_m, β, κ, and $D(\xi)$. We assume that $D(\xi) = D_0 + D_1\xi$, where D_0 and D_1 are determined by calibration.

Efficient Routing. The routing uses D∞ paths and slopes calculated using TauDEM, at a high resolution compared to the weather inputs (for the Bhakra basin, a 1 km resolution). For computational efficiency, these paths are aggregated to the lower resolution of the weather inputs using a network structure as explained below.

Each node j in the flow network is characterized by an effective length in the direction of streamflow (L_j), and spatial characteristics for determining flow rates. At each timestep, each node j contains a volume of water $W_j(t) = \int_0^t (\Delta Q_j^{in}(\tau) - \Delta Q_j^{out}(\tau))d\tau$, where $\Delta Q_j(\tau) = \Delta Q_{R,j}(\tau) + \Delta Q_{M,j}(\tau)$. The correspondence between grid cells i and nodes j is shown in figure 2.

Flows into and between nodes are calculated in time steps that satisfy the Courant condition. Let the flow velocity of node j in time t be $v_j(t)$. For each timestep, Δt, runoff flows a distance $v_j(t)\Delta t$, and the volume $W_j(t)\frac{v_j(t)\Delta t}{L_j}$ exists the node. This volume of outflow is distributed amongst receiving nodes according to D∞ flow directions.

Flow velocities are calculated from the Manning formula,

$$v_j(t) = \frac{1}{n_j} r_j(t)^{2/3} s_j(t)^{1/2}$$

where the parameters are calculated differently for "surface" nodes and "channel" nodes.

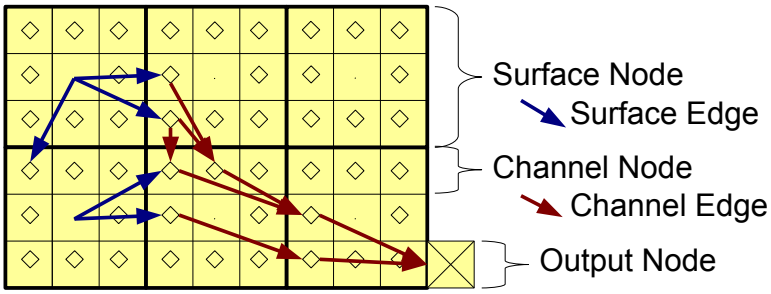

Figure 2: Simple network flow model. Blue lines represent flow of surface nodes, red for channel node flow.

Each surface node corresponds to a grid cell at the resolution of weather data. Each surface node is connected to one or more channel nodes, based on the possible paths water could flow out of that grid cell. Rainfall and melt for each time-step are initially allocated to the surface nodes. The Manning formula for surface nodes uses $n_j = 0.025$ (Te Chow, 1959) and $r_j(t) = \frac{W_j(t)}{A_j}$ where A_j is the node's area. The value for $r_j(t)$ follows from the assumption that the base the channel is much wider than the depth of the flow, so $r_j(t)$ is approximately the depth of flow. The edges connecting surface nodes to channel nodes are weighted by the number of high-resolution grid cells that drain into each possible channel, and L_j is the average distance traveled to the edge of the grid cell.

Each channel node corresponds to the possible paths streamflow could take from the edge of a grid cell to a neighboring grid cell. There could be more than one path, if the D∞ angles specify ambiguity between any of the paths at the high resolution. Each channel node can be fed by one surface node and multiple channel nodes. The Manning formula for river nodes uses $n_j = 0.033$ (Te Chow, 1959) and the $r_j(t)$ for a filled half-cylinder with width equal to the effective width of the channel node. Edges between channel nodes are weighted by the portion of streamflow specified by the composite effects of the D∞ angles, and L_j is determined by the total distance traveled to get from one edge of the grid cell to another.

For all nodes, the effective slope for determining flow velocity is,

$$s_j(t) = \max\left(\bar{s}_j, \frac{H_j(t)}{2L_j}\right)$$

where $\bar{s}_j$ is the slope of the topography, $H_j(t)$ is the depth of flow (using the same geometry as the hydraulic radius calculations).

The weights on edges between nodes determine the portion of water volume at a node which goes to each of the nodes it is connected to. Specifically, each time step, the flow from node j to node k is,

$$F_{jk} = v_{jt}\frac{\Delta t}{L_j}\frac{w_{jk}}{\sum_l w_{jl}}V_{jt}$$

where Δt is the time step, w_{jk} is the weight from node j to node k (as defined above), and V_{jt} is the volume of water currently represented within node j.

The volume at node j in the next time step is then,

$$V_{j,t+1} = V_{jt} - \sum_k F_{jk} + \sum_l F_{lj}$$

Evapotranspiration, modeled either a simple temperature curve or a simplified version of the Penman equation, was considered in the model as well, but its contribution was not significant.

3. Data and Calibration

The Bhakra basin covers 58683 km^2, with elevation ranging from 515 m (above m.s.l.) to 4570 m. Reservoir inflow measurements are available starting in 1963, when the dam was built. This data has previously been analyzed for its monthly streamflow from melt Singh and Jain (2002, 2003) and climate impacts on flows (Singh and Bengtsson, 2004, 2005, Pal et al., 2012a) and flow predictability Pal et al. (2012b).

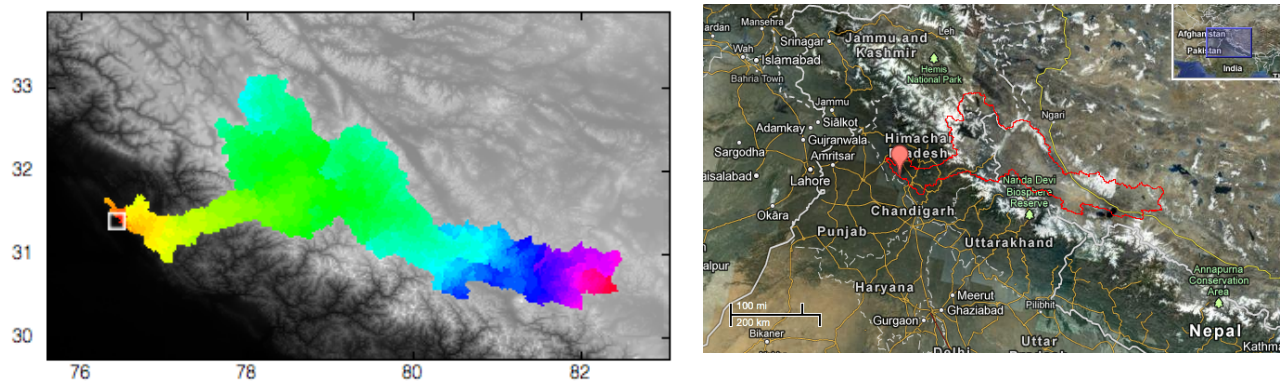

Figure 3: Bhakra dam basin (white box) and its catchment basin. Colors show approximate relative travel times for runoff.

Streamflow Data: Bhakra dam inflow measurements were provided by the Bhakra Beas Management Board of India (BBMB), from 1963 to 2005.

Basin Topography: Basin topography is from NOAA NGDC's Global Land One-km Base Elevation (GLOBE) Digital Elevation Model (Version 1.0, 1999).

Precipitation Data: Daily precipitation is merged from three sources: NASA's Tropical Rainfall Measuring Mission (TRMM), algorithm 3B42 (1998 to 2011, .25°x.25°), the NCC1-2008 High Resolution Gridded Precipitation Data Set (1901 to 2004, 1°x1°), and the India Meteorological Department's 0.5 Degree Daily Gridded Precipitation (RF0p5) Data Set, (1971 to 2005, .5°x.5°). The three precipitation products were combined to provide full spatial and temporal coverage (see Supplement A).

Temperature Data: Daily temperature is from the India Meteorological Department High Resolution Daily Gridded Temperature (HRDGT) Data Set (1969 to 2005, 1°x1°) and NOAA NCEP/NCAR CDAS-1 Reanalysis project (1948 to 2011, 1.875°x1.904726°). Again, these provide full coverage, and the merging process is detailed in Supplement A.

Snow/Ice Cover: Weekly snow/ice cover data is from NOAA NCDC SSM/I (1988 to 2003, .333°x.333°) from Grody and Basist (1996). For years before 1988, the 1988 data is used.

The flow model is estimated from TauDEM D∞ flow directions and the network optimization described above, and is displayed in figure 4.

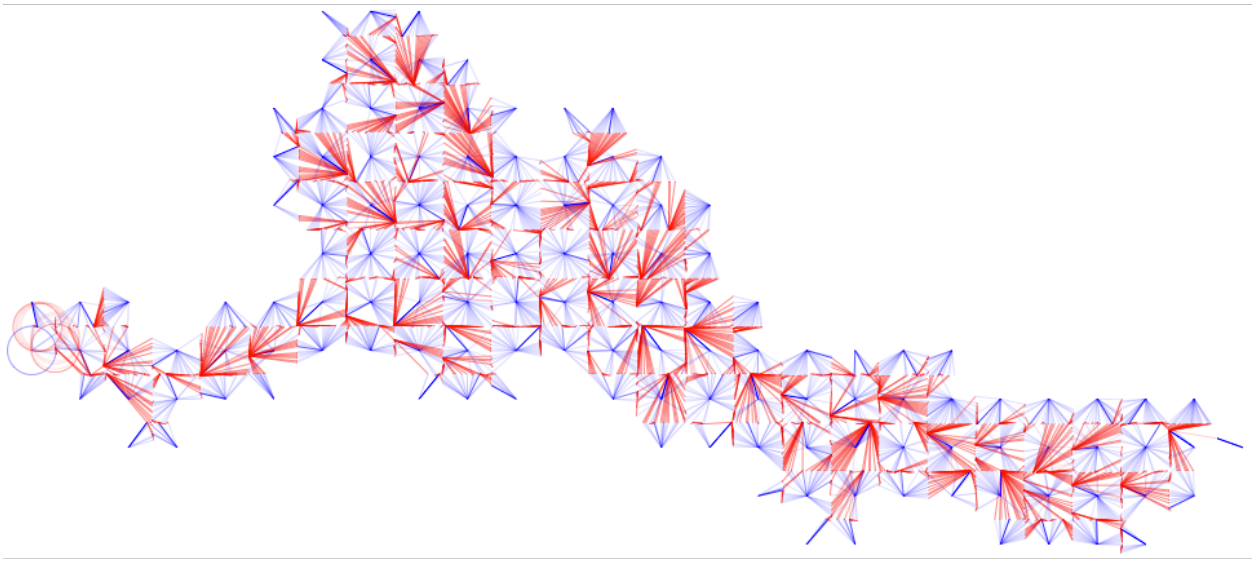

Figure 4: Flow paths, .25° resolution based on .0083° resolution D∞ directions. Blue lines represent flow of surface nodes, red for channel node flow.

The model is calibrated to maximize the R^2 of the predicted streamflow, using the ten years 1988, 1989, and 1992 - 1999. 1990 and 1991 were excluded due to missing snow cover data. The remaining years, 2000 - 2003, are used for validation. The optimization method is an evolution strategy, as described in supplement B. Our calibration maximizes R^2 while allowing for efficient exploration of the parameter space and tunneling toward a global optimum.

The resulting flows, compared to the measured Bhakra inflows, are shown in figure 5.

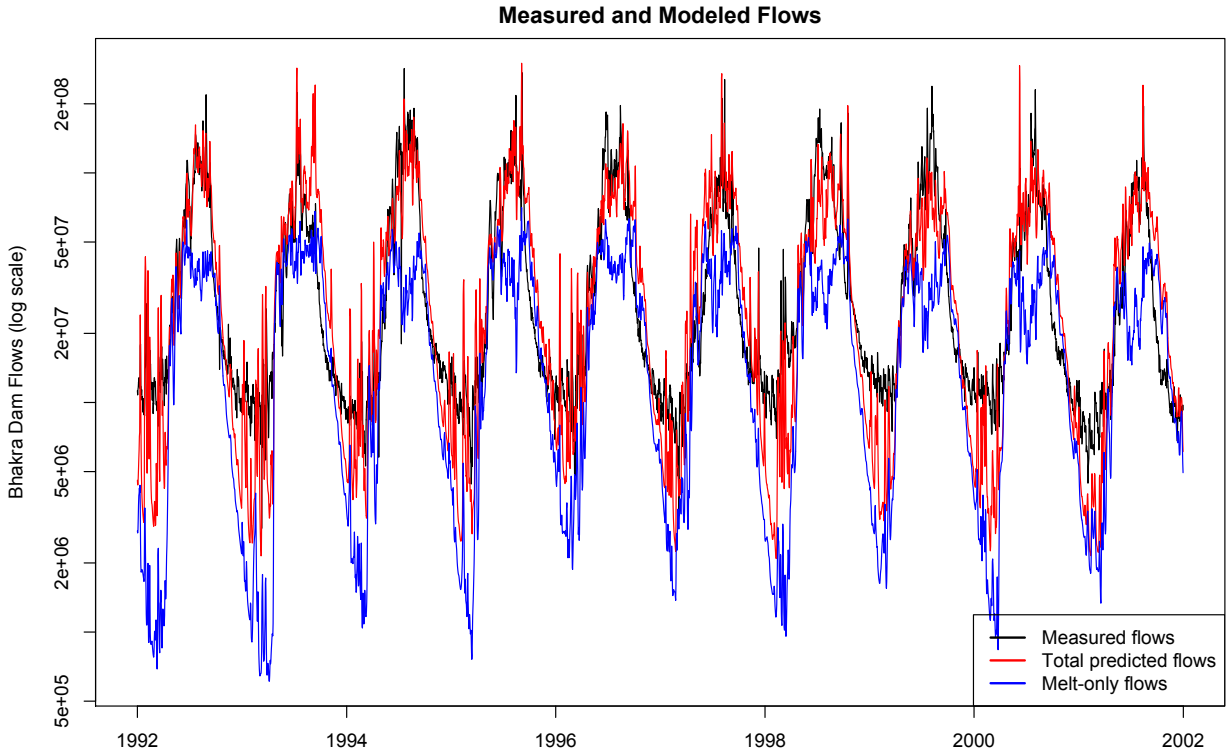

Figure 5: Measured streamflow compared to estimated streamflow components, 1992 - 2001. Bhakra inflows (black) and modeled melt flows (blue) and combined melt and precipitation flows (red).

The calibrated coefficients are $D_0 = 3.08558$, $D_1 = -0.00011$, $C_r = 0.02804$, $C_m = 0.01148$, $\beta = 0.00899$, and $\kappa = 0.02817$. The value of D_0 is less than measured values for the region, such as 5.7 - 8.0 $\frac{mm}{^\circ C day}$ for the Dokriani Glacier, but within the range of degree-day factors for snow across the literature of 3 - 5 $\frac{mm}{^\circ C day}$ (Singh et al., 2000). The runoff coefficients, at 1.1% and 2.8% are smaller than expected, probably reflecting excessive rainfall inputs, from the coarse estimates available through remote sensing.

The resulting fit has an $R^2 = 0.68$, the sum of melt and precipitation flows have a Pearson's correlation with the true flows of 0.83, and the error has $n - 6 = 3647$ degrees of freedom. Validation tests are shown in figure 6. Over the four validation years, $R^2 = 0.52$ and correlation is 0.75. Over the entire range of years used for flood analysis, 1963 - 2004, $R^2 = 0.57$ and Pearson's correlation is 0.77.

Daily modeled flows fall within 95% confidence intervals 0.232 and 2.313 of the measured values.

Flood Analysis

Floods are estimated using a "volume over banks" measure. The median yearly peak flow, Q_{50}, is taken as the threshold for a streamflow to be considered a flood. The flood volume

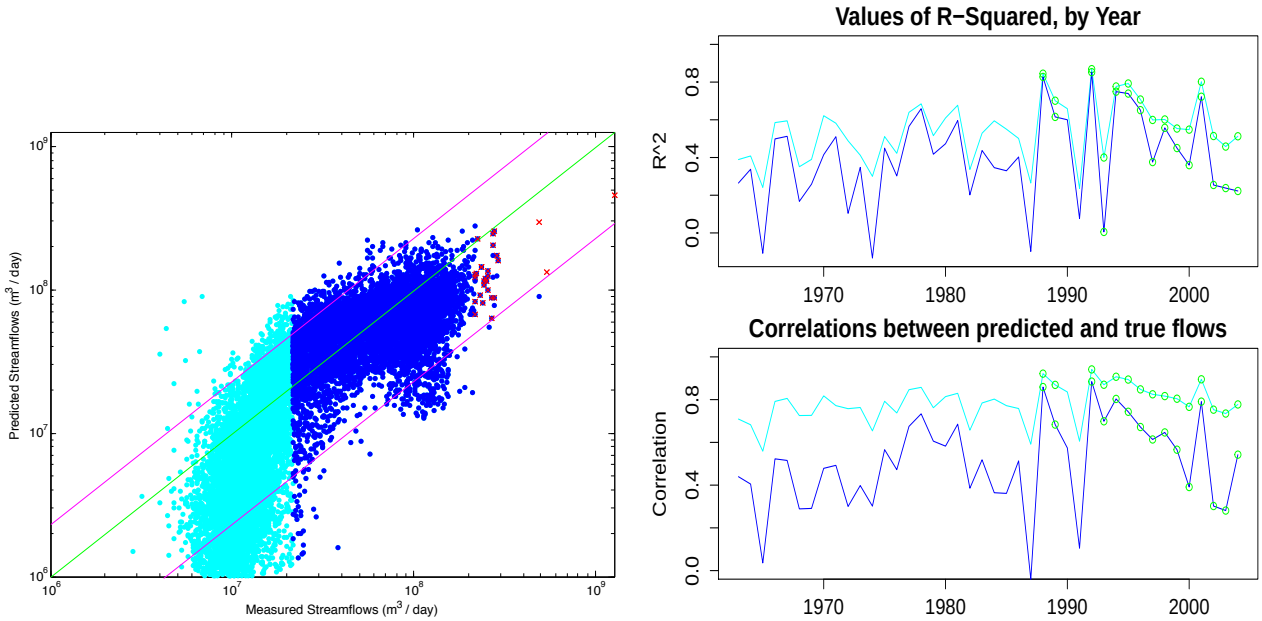

Figure 6: The left scatter plot shows modeled streamflow at the Bhakra Dam vs. measured inflows, in logs. Each blue or cyan dot is a daily observation. Floods, as defined in section 3, are marked by red x's. The purple lines show 95% confidence intervals. Cyan dots are below 10% of the flood threshold and are not used for the confidence bound calculation. The right plots shows values of R^2 and correlation of the fitted model by year. Cyan shows the skill over all daily observations, blue for only values over 10% of the flood threshold. Snow data is available for years with green circle.

is then the sum of this exceedance over days:

$$V_{flood} = \sum_{t \text{ while } Q_t > Q_{50}} K(Q_t - Q_{50})$$

for some conversion factor K. $K = 1$ for Q_t measured in m^3/day.

By this definition, there are 28 floods, with some years having multiple floods. $Q_{50} = 2.1619e8\ m^3/s$. Figure 7 shows these floods.

The model estimates the separate contributions of melt and precipitation. Figure 8 shows each flood and the size of its contributing factors.

To estimate the portion of the 10-year and 100-year flood attributable to rain and melt, we used a Gaussian copula. The univariate density functions were estimated empirically using a log-normal kernel, to capture the extreme values displayed in the graph. We estimated the 10-year and 100-year floods and 95% confidence intervals from 100 bootstrapped samples, each fit to a copula, and 1000 draws of the copula's distribution. The portion attributable to melt is estimated as the melt volume divided by the sum of the precipitation and melt volumes.

We also estimate 95% "total confidence" intervals, accounting for uncertainty in the model. These provide wide bounds, if the uncertainty calculated due to variance in the estimates is

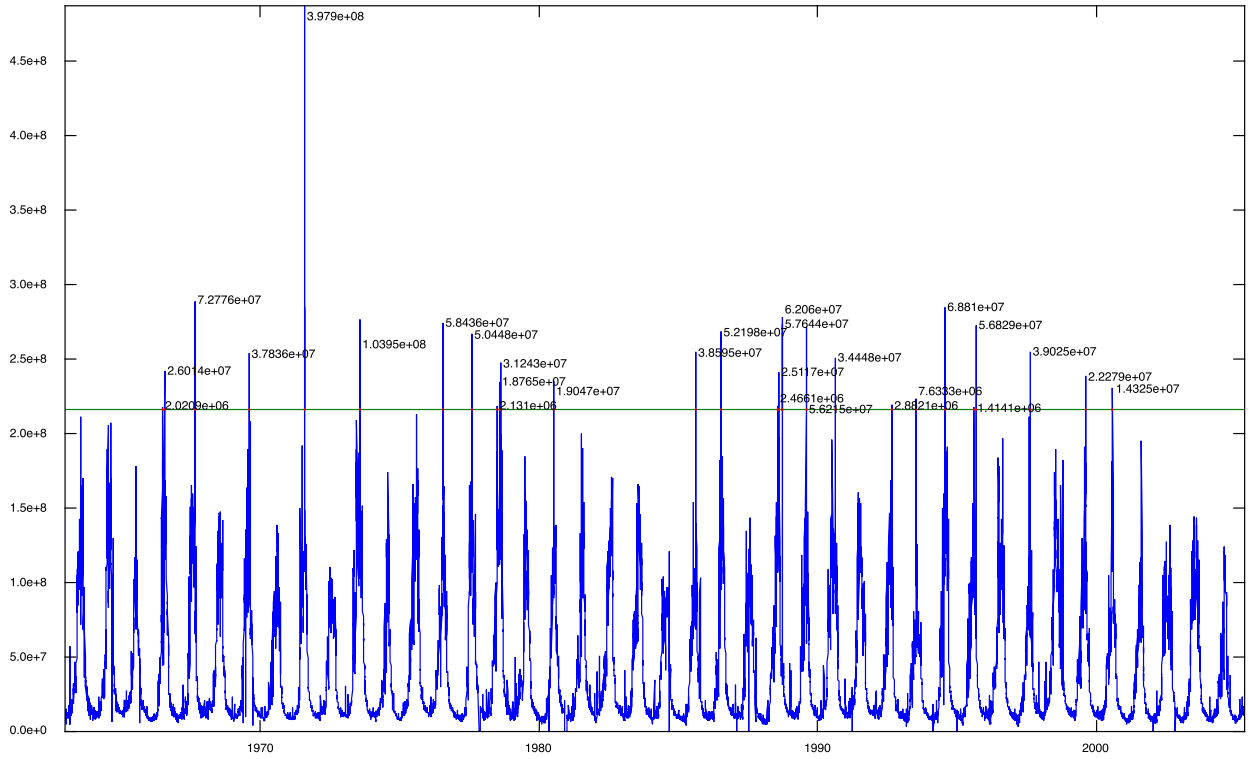

Figure 7: Measured floods, shown with volumes (in m^3), at the Bhakra dam. Floods quantified as "volume over banks" (medium year max flow). These are compared to the combined precipitation and melt flow estimated by the model.

independent of uncertainty due to model results. Calculations are provided in supplement C. The results are displayed in the table below.

Model	Estimate	95% CI	95% total CI
Mean of Historical Floods (N=28)	22.2%	10.8% - 40.6%	5.6% - 69%
Mean of 10-year Historical Floods (N=5)	19.6%	4.2% - 63.8%	5.7% - 62%
Copula Model, 10-year Flood	19.4%	12.7% - 31.6%	4.1% - 76%
Copula Model, 100-year Flood	20.2%	15.5% - 27.3%	4.4% - 76%

The effect varies over the basin, with larger portions due to melt upstream. We repeat the process for each modeled grid cell, recording the maximum yearly flow into each cell, identifying the "volume over banks" floods, and fitting a copula model with the associated melt and rain flows. The resulting portions are shown in figure 9.

By applying the calibrated physical model to the entire Himalayan region, we can estimate the portion of the 10-year flood attributable to melt across the region.

Figure 10 shows that the increased melt contribution extends into rivers, on the southwest (30%) and southeast (10-20%).

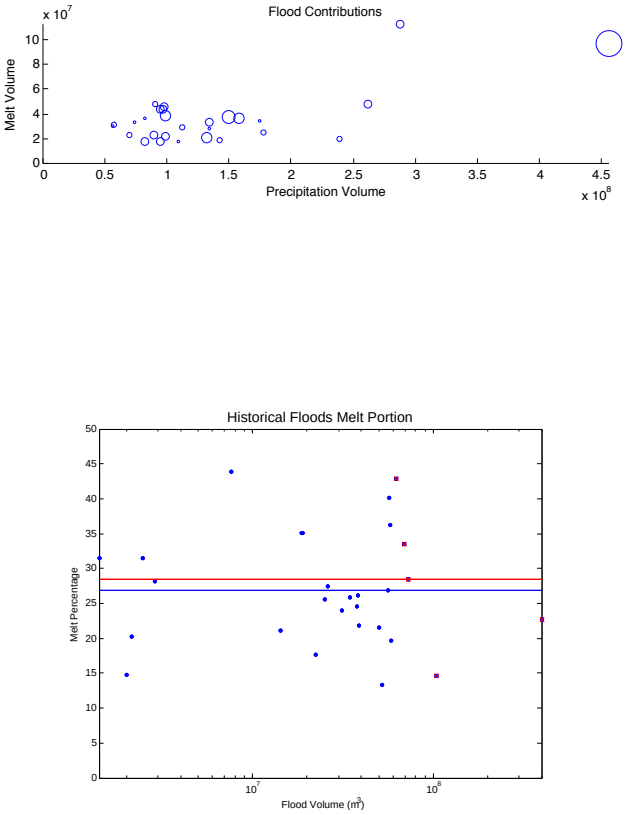

Figure 8: Contributions to floods. On top, sizes of circles show relative flood size. On bottom, the fraction of the estimated streamflow attributable to melt is plotted vs. the flood size. The green line shows mean fraction for all floods and the red shows mean fraction for the historical 10-year flood (the top 5 from the 53 year dataset).

Sensitivity Analysis

Following Singh and Bengtsson (2004), we analyzed model sensitivity by estimating results for uniform changes to temperature and precipitation.

For temperature, we ran the model with inputs of temperatures at $T + .5$, $T + 1.0$, $T + 1.5$, and $T + 2.0$. Because the model uses temperature-based melt calculations, and does not estimate snow volume, melt volumes necessarily increase under these scenarios. Streamflow from precipitation also increases slightly, as more precipitation falls as rain.

For precipitation, we applied multiplicative increases of $1.1P$, $1.2P$, $1.3P$, and $1.4P$. This corresponds to the range of annual precipitation increases expected over much of the South Asia region (Solomon et al., 2007).

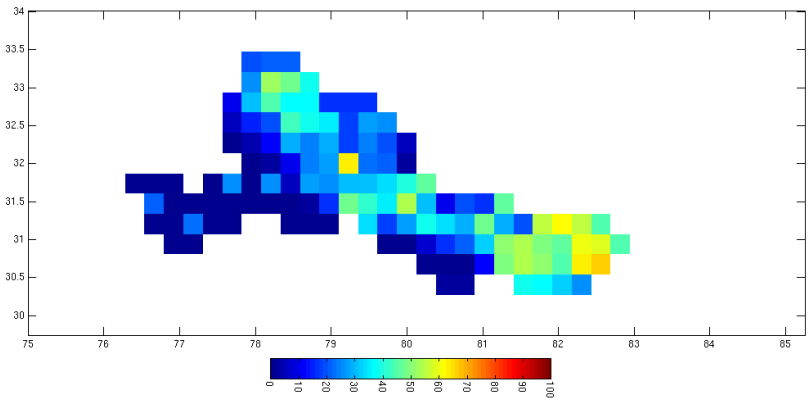

Figure 9: Portion of 10-year flood attributable to melt, over the Bhakra basin.

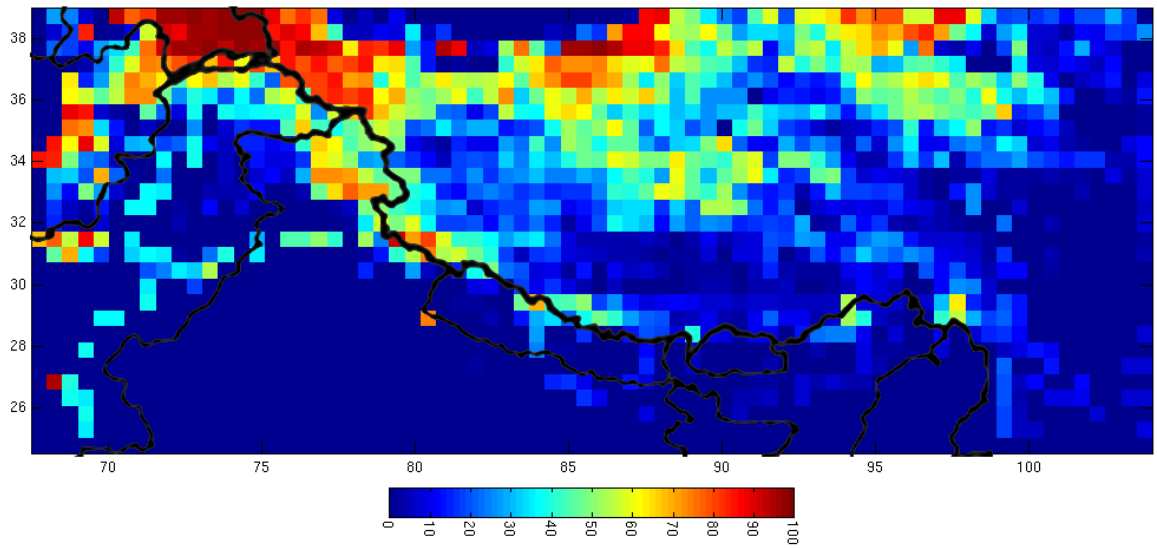

Figure 10: Estimation of flood portion attributable to melt across the entire Himalayan region.

The changes can be seen by considering the size of the historical 10-year flood (taken to be the top 10 floods over the 53 year period.

Temperature		Precipitation	
	Mean top 5 (m^3)		Mean top 5 (m^3)
Measured	5.13e8	Measured	5.13e8
Base Model	4.02e8	Base Model	4.02e8
T+0.5°C	4.08e8	1.1 P	4.35e8
T+1.0°C	4.15e8	1.2 P	4.69e8
T+1.5°C	4.21e8	1.3 P	5.03e8
T+2.0°C	4.27e8	1.4 P	5.37e8

The 10-year flood increases by 12.5 MCM (a 3.1% increase) per °C and 33.5 MCM (a 8.4% increase) per 10% increase in precipitation.

We also estimate the historical 10-year flood in the absence of snow. Under this scenario, the 10-year flood is 3.53e8 m^3, a decrease of 12% or 48.9 MCM. This is smaller than the portion of flood due to melt because decreases in melt cause increases in runoff, similar to the result in (Kaser et al., 2003).

For each change in weather inputs, we produce bootstrapped copula estimates of the melt portion in 10-year and 100-year floods. The result is approximately linear across weather changes. We estimate the effect with a linear regression:

$$P_i = \beta_0 + \beta_1 \Delta X_i + \epsilon_i$$

where P_i is the portion of a flood from melt under a given model run, and ΔX_i is the model run weather factor.

Figure 11 shows a histogram of copula estimates of the melt portion of the 10-year and 100-year flood. Each histogram is produced from multiple draws of a copula fit to a single model run with the given change in weather (shown in between the two columns).

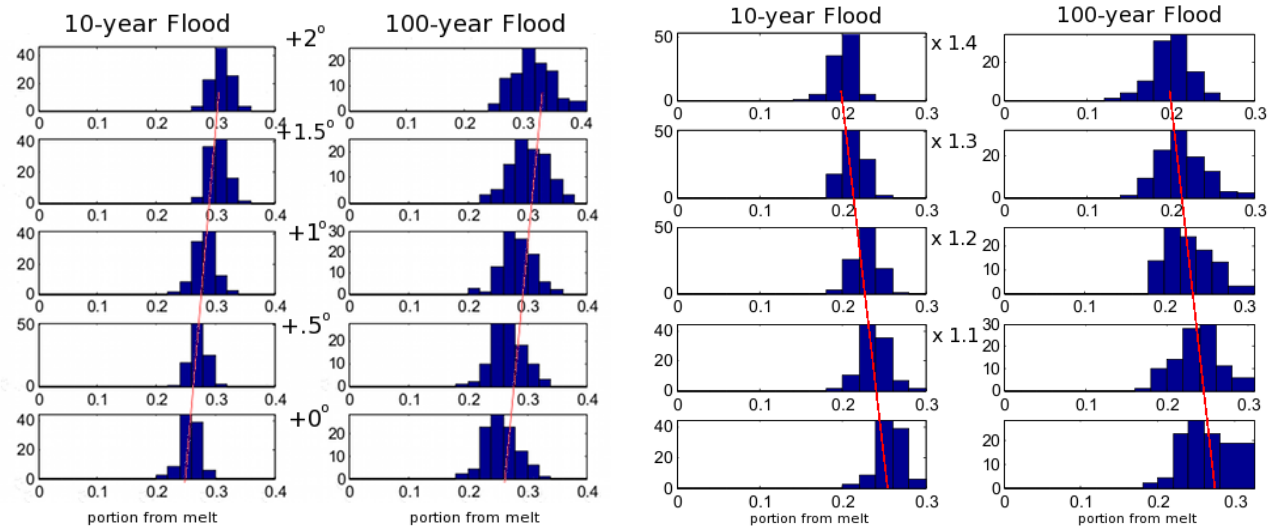

Figure 11: Estimates of the portion of the 10-year and 100-year flood attributable to melt, under uniform additive increases in temperature (left) and uniform multiplicative increase in precipitation (right). .

Coefficients	constant	ΔT	(R^2)
10-year	.2577	0.0275	(.608)
100-year	.2543	0.0312	(.365)
Coefficients	constant	ΔP	(R^2)
10-year	.2554	-0.0280	(.650)
100-year	.2541	-0.0268	(.341)

4. Conclusion

The implications of flooding have been discussed by many authors. Ahern et al. (2005) provides a survey of the epidemiological effects of flooding, while Kundzewicz and Takeuchi

(1999) provide an overview of the history of flood control and mitigation, and suggest the idea of "living with floods." The framework for how to manage the hydrological effects of climate change needs further development (Wescoat Jr, 1991).

This paper introduces a distributed physical model, allowing the hydrological effects of climate change to be investigated with minimal data available through remote sensing, and across wide landscapes.

Flooding is becoming an increasingly pressing issue. Changes in the severity of floods are a result of a wide range of factors, not limited to climate or weather. Changes basin management, vegetation cover, and infrastructure all play a large role. This study finds that snow andice melt contribute about 26% of the volume of historical floods at the Bhakra dam. While this portion are highest in snowy regions, it remains significant along snow-fed rivers like the Indus. Depending on winter accumulation patterns, spring melt-rates, and decreases in the extent of glaciers, the size of catastrophic floods may change significantly.

One possible explanation for this considerable portion is that catastrophic floods represent a combination of an unlikely precipitation event and an unlikely temperature (melt) event. However, we estimated a statistical, analytical model to investigate this and found that variability in temperature cannot explain the increase (see supplement E). Instead, it appears to be due to a kind of "flushing out" of resident melt water throughout the basin.

By applying our climate sensitivity tests to expected climate trends (as predicted by CCSM 3.0 under the A1B scenario), we find that by 2050, the annual flood season will produce two kinds of flood behavior, due entirely to changes in melt. In years where large precipitation events coincide with the spring melt, large (10-year) floods will be 6% larger (2 - 17%). In years where large precipitation events occur after all winter accumulation has melted, the 10-year flood will be 12% (4 - 32%) smaller.

5. Acknowledgments

Many thanks to John Mutter, Indrani Pal, and Johanna Goetzel.

Appendix A. Merging Weather Data

Temperature and precipitation was combined from multiple sources to ensure coverage of the entire basin between 1963 and 2005. All of the data sources are satellite or reanalysis products.

Precipitation Data Sources			
CDAS	NOAA NCEP-NCAR CDAS-1	1963 to 1998	1.875°x1.904726°
NCC1	NCC1-2008 High Resolution Gridded Precipitation Data Set	1963 to 2004	1°x1°
RF0p5	India Meteorological Department 0.5 Degree Daily Gridded Precipitation	1971 to 2005	.5°x.5°
TRMM	NASA's Tropical Rainfall Measuring Mission, algorithm 3B42	1998 to 2005	.25°x.25°
Temperature Data Sources			
CDAS	NOAA NCEP/NCAR CDAS-1 Reanalysis	1963 to 2005	1.875°x1.904726°
HRDGT	India Meteorological Department High Resolution Daily Gridded Temperature	1969 to 2005	1°x1°
CAMS	NOAA NCEP CPC GHCN-CAMS	1963 to 2005	.5°x.5°

To merge the data, we resampled all products to a .25°x.25° grid. For each year and each grid cell, we consider the merged temperature to be a weighted average of all available data. The

complexity of mountain topography produces rapid changes in precipitation and temperature over short distances (Becker and Bugmann, 1997), so more weight was placed on datasets of higher resolution where they overlap.

In addition, for temperature, we applied a 6.5°C / 1000 m temperature lapse, adjusting the temperature of each high-resolution grid cell against that original datasource's grid cells mean temperature. Finally, we used CAMS to provide a common baseline temperature, and applied deviations of each grid cells temperature from that grid cells monthly mean to get the final grid cell temperature.

To diagnose the degree of agreement between different sources, we looked at the yearly mean and variance across the region all sources share, the residuals around the mean and average variance as they vary by month, and the correlation of each source with the combined result, across space. See figure 12.

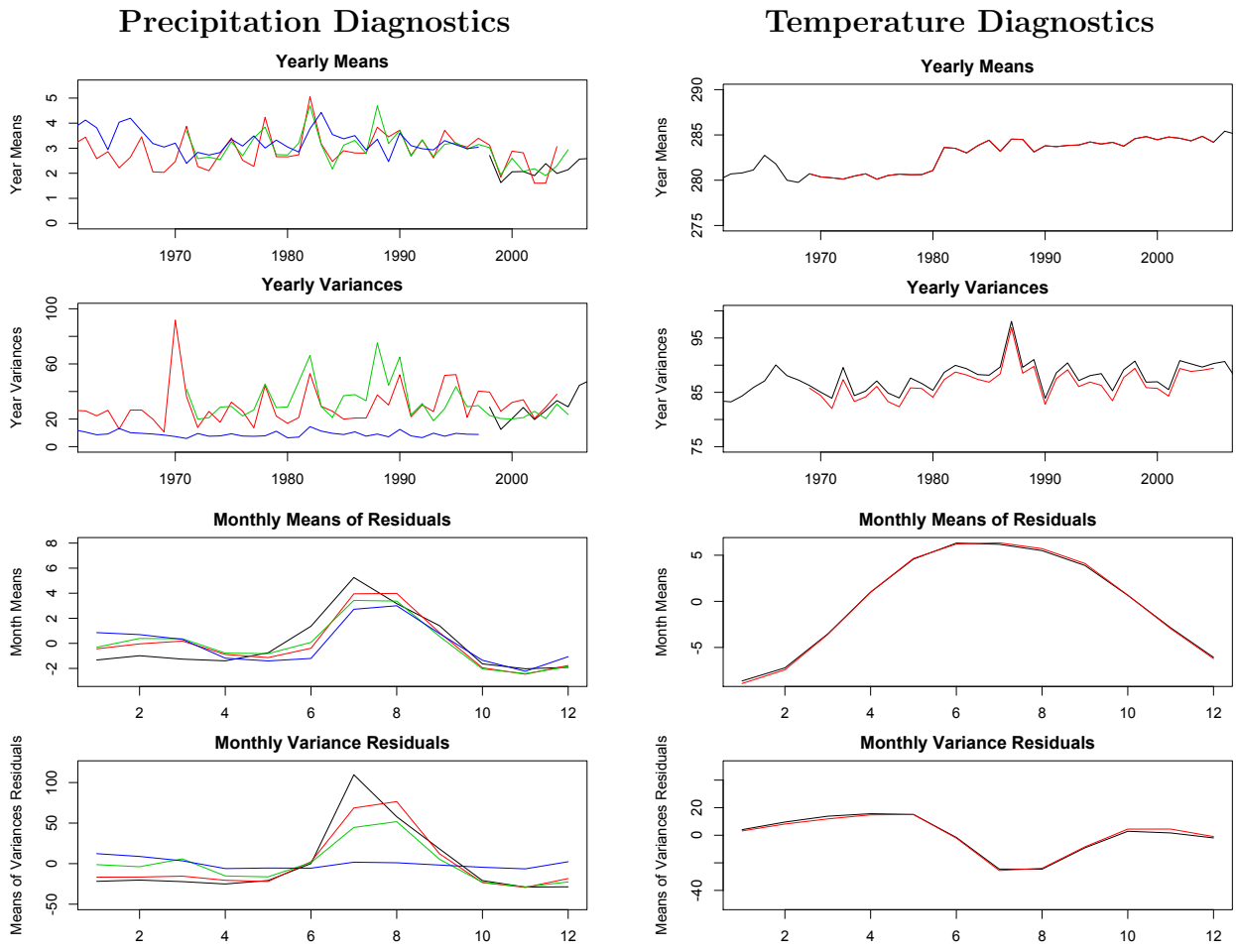

Figure 12: Diagnostics for the fit between different data sources of precipitation and temperature. All diagnostics do very well on temperature produces. Precipitation products are more problematic, the greatest problem being the mismatch of the CDAS dataset, blue (which is given a weight 30 times less than the other datasets).

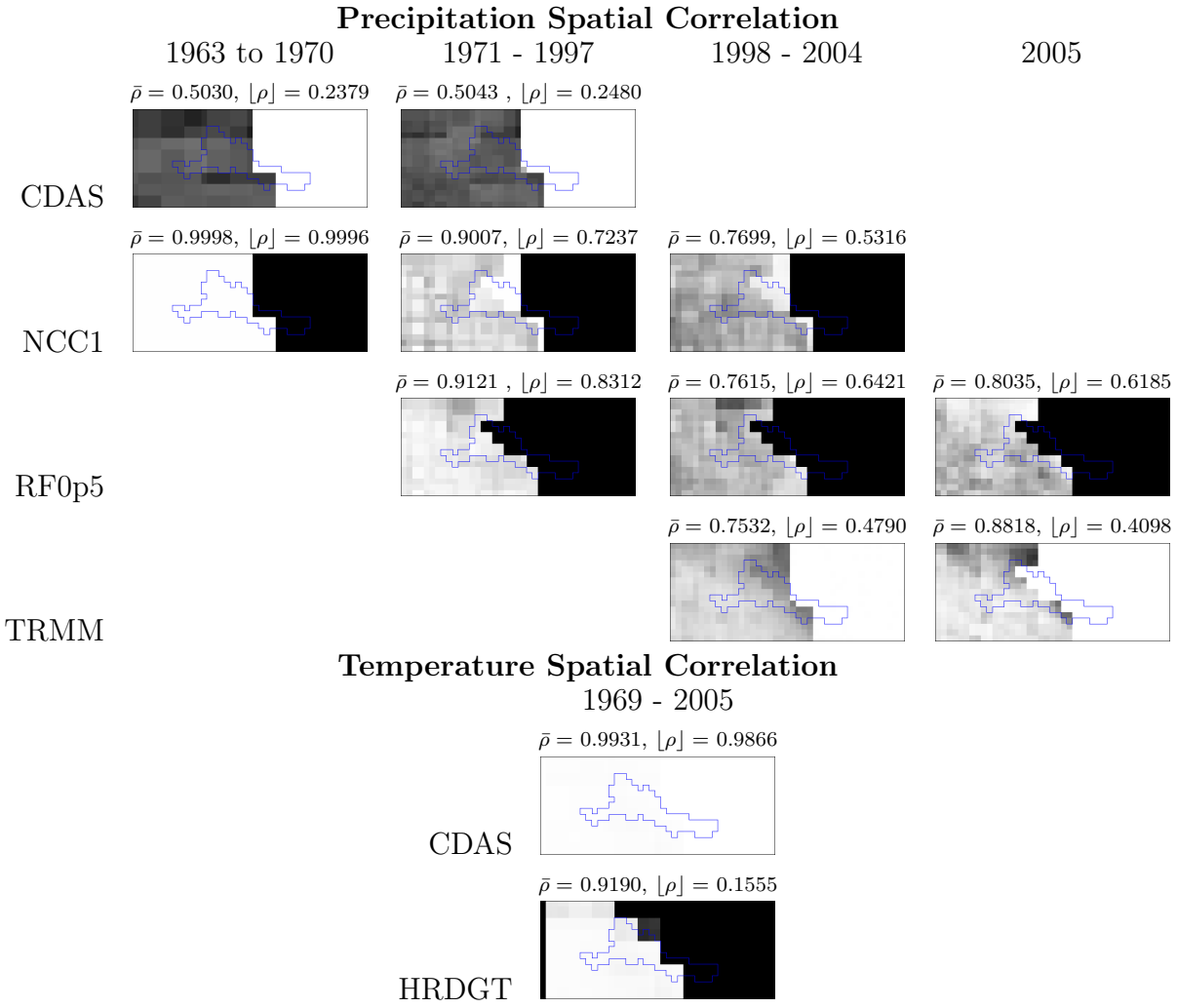

Figure 13 displays a useful metric for understanding how impact of melt on streamflow varies across a region. We define the basin of a grid cell as the region that drains to that point, and allow cells to be fractionally included if the D∞ flow directions specify that only a portion flows into the grid cell. The melt metric is the ratio of the average annual snowcover across a gridcell's basin to the total area of its basin. This measure is always between 0 and 1.

In most regions, the metric corresponds very closely to the average annual snowcover. However, along major snowfed rivers, the measure remains high, despite the long distance from snow-covered regions. This supports the finding in the paper that a melt constitutes a high portion of major floods far along melt-fed rivers.

Snow cover decreases yearly, reaching a minimum around the time when major floods are most likely (see figure 14). This may be partly driven by decreases in the snow buffering effect, where less snowcover results in greater runoff. It also suggests that flood size is sensitive to additional climate change: further decreases in summer snowcover can remove the entire melt component from floods.

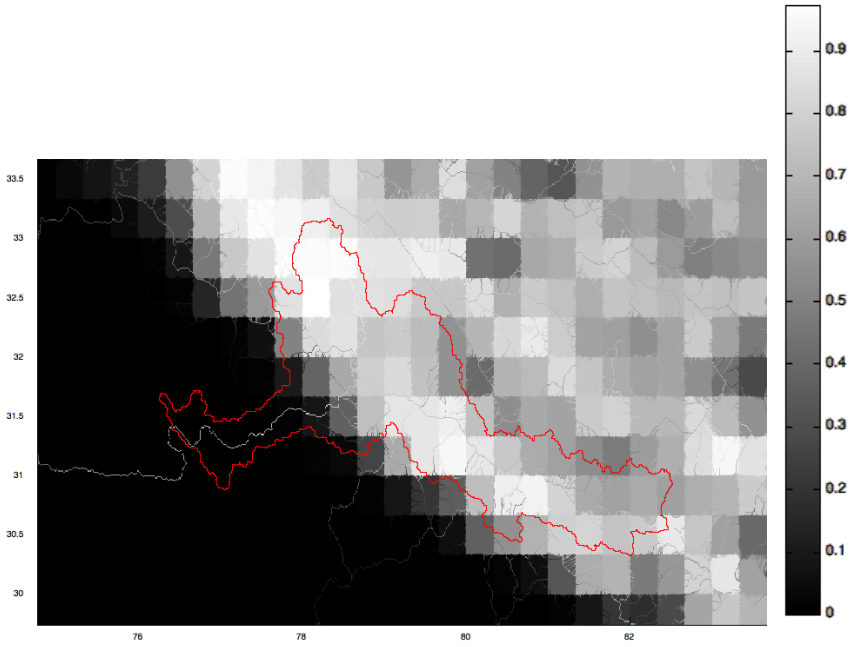

Figure 13: Measure of annual snowcover to total basin area, by grid cell.

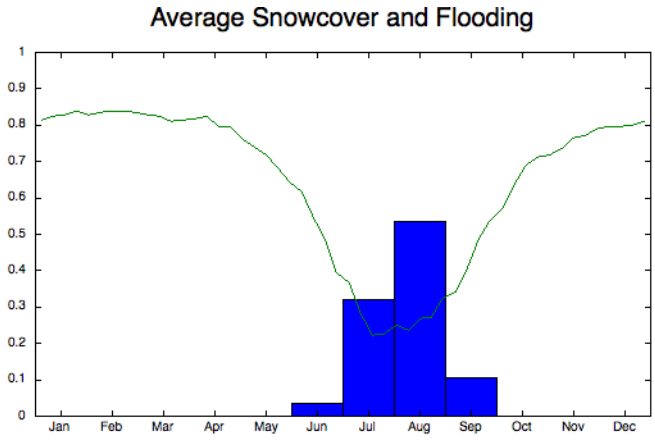

Figure 14: Average Bhakra basin snowcover (green) and historical floods (blue). Floods are identified as sustained flows above the median of yearly peak flows.

Appendix B. Model Calibration

We used an evolutionary strategy to fit the model. The method maintains a population of 10 parameter value sets. At each step, an "offspring" is generated from one of these existing parameter sets, by drawing from a Gaussian sphere surrounding that parent. Its fitness is then determined by the R^2 of its prediction of a single year's streamflow (for computational speed). The parent's recorded fitness is adjusted slightly to approach its offspring's, and the

offspring is accepted into the population if it has a greater fitness than one of the existing parents. Step sizes gradually decrease by adjusting the variance of the Gaussian sphere.

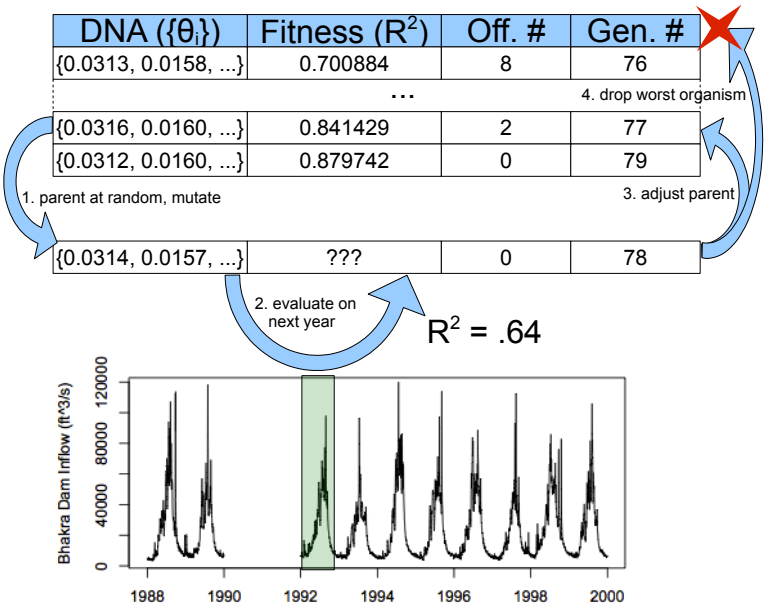

Figure 15: Steps in the evolutionary strategy process. 1. A random parent is selected from the existing population, and an offspring is generated by a mutation. 2. The offspring is evaluated by determining its R^2 prediction for a single year. 3. The parent's R^2 fitness is adjusted to approach the offspring. 4. If the offspring's fitness is greater than the worst member of the population, the offspring is added and the worse member dropped; otherwise, the offspring is dropped.

Validation of the results is shown in the paper. Figure 16 shows additional diagnostics. A large source of error is probably the use of remote-sensing precipitation data, which can have poor performance in mountainous regions with complex hydrology.

Appendix C. Calculations for Estimating Flood Portions

Three estimates are used to determine the average and confidence intervals on the portion of the 10-year and 100-year floods attributable to melt.

Confidence intervals for historical floods are based on a posterior Beta distribution, formed by the a prior uniform(0, 1) distribution and a traditional binomial distribution.

For the copula-based estimate, we estimate the joint dependence between precipitation volume, melt volume, and flood volume. For historical floods, measured flood sizes are used; for sensitivity checks and portion maps, modeled flood sizes are used. Draws from the joint probability model are displayed in figure 17.

The 10-year flood was estimated as the 80th-percentile of 1000 draws, and the 100-year flood is the 98th-percentile. The 80th-percentile is used (rather than the 90th-percentile), because a flood occurs on average only every 2 years. For producing bootstrapped confidence

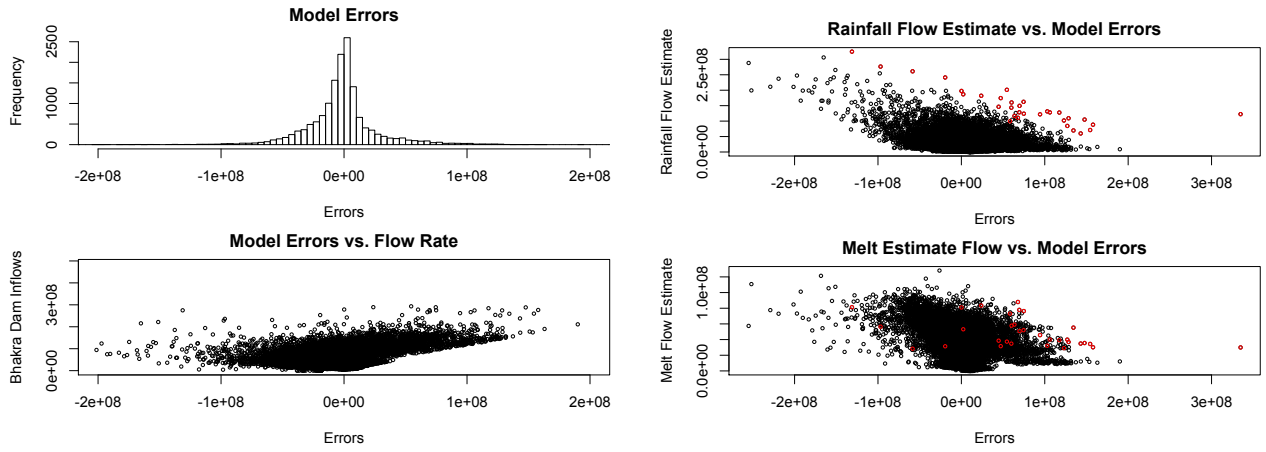

Figure 16: The left figures show the spread of errors (measured - predicted), which are approximately symmetric, but the model tends to overestimate medium-sized flows and underestimate large flows. The right figures display the melt portion vs. the model errors, and highlight historical floods in red. While the melt estimates for large floods tend are within the range of melt estimates for daily flows (lower graph), precipitation estimates of large floods are almost always greater than other flows with the error.

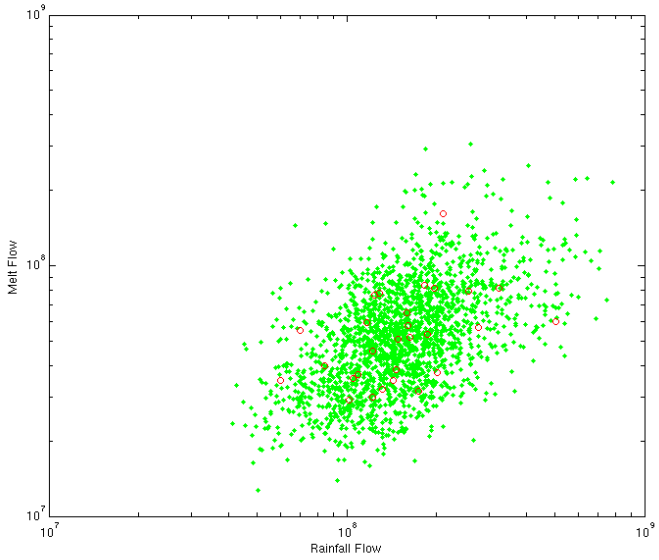

Figure 17: Draws from the joint probability model, in green. Red circles identify historical floods.

intervals, floods were sampled with replacement, fitted to a new copula model, and the 10-year and 100-year sizes were estimated.

Finally, the uncertainty of the modeling process was added to the uncertainty in the other estimates to produce a "total confidence interval" estimate, using an *inexact Gaussian theory* estimate (Menke, 2012).

We take a constant prior on $\log q_{melt}$, up to 1. The variance in our data is, in this case, the variance amongst estimates of the 10-year or 100-year flood size. The uncertainty in the theory is the Gaussian variance of the error between modeled inflows and measured inflows.

$$p(\log q_{melt}) \propto 1 \text{ for } q_{melt} \leq 1$$
$$p(\log q_{obs}) \sim N(\log \bar{q}_{obs}, \sigma^2_{obs})$$
$$p(\log q_{melt}, \log q_{obs}) \sim N(\log q_{obs} - \log q_{melt}, \sigma^2_{err})$$

where q_{obs} is the original estimate of the portion due to melt, with a variance, σ^2_{obs}, given by the binomial approximation or bootstrapped results, and σ^2_{err} is the variance in the difference between estimated and observed daily inflows.

The final distribution is the clipped Gaussian,

$$p(\log q_{melt}) \sim N((\sum_i \log p_i)/N, \sigma^2_{obs} + \sigma^2_{err})[-\infty, 0]$$

Appendix D. Additional Data Analysis

The GLOBE digital elevation model provides a spatial resolution of 1km x 1km, and 1 meter elevation resolution, but because it was derived in part from cartographic sources, which can result of contour line artifacts, and has the potential for up to ± 250 m errors. Applying the same criteria as the GLOBE report, this histogram identifies elevation data artifacts (see `http://www.ngdc.noaa.gov/mgg/topo/report/plates/p27a.html` for the histogram for Southeast Asia). Elevation data appears to be reliable over the flood extent map; see figure 18.

We use TauDEM to generate D∞ flow directions and slopes. The results are shown in figure 19.

By averaging precipitation, snow cover, and temperature over the entire basin, we can see clear connections between high daily inflows at the Bhakra dam and the other variables. Almost all Bhakra inflows over 20000 ft^3/s occurred on days with an average temperatures greater than 12°C. While snow cover tends to be low on such high-temperature days, the great majority of such days had some snow, and some as much as 50% snow cover. The correlation between streamflows and precipitation is 0.389, between streamflows and temperature is 0.719, and between precipitation and temperatures is 0.201.

Over the time period from 1963 to 2004, the Bhakra basin has had no significant trend in average temperature, but showed a decreasing trend in precipitation and precipitation variability (as measured by the day-to-day variance). We compared these trends predicted data from CCSM 3.0 under the A1B IPCC scenario (generated by NCAR for the IPCC AR4), between 2000 and 2050. The predicted data shows a positive trend in temperature and a negative (but insignificant) trend in precipitation and precipitation variance (see figures 21 and 22). All of these suggest that over the next 50 years, melt has the potential to be a greater component of floods, unless available snow cover becomes a limiting factor.

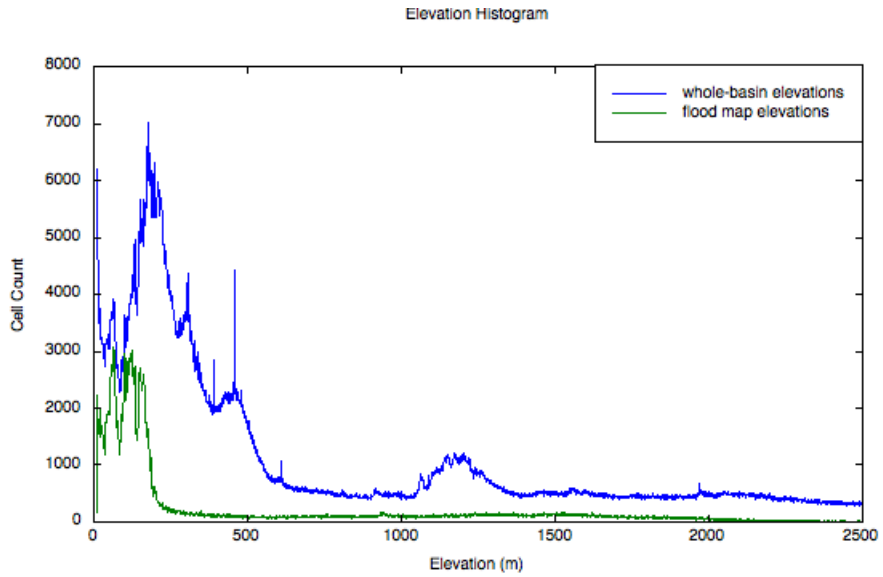

Figure 18: The histogram of elevations allows for inaccuracies in the DEM to be diagnosed. The histogram over the entire region shows clear spikes near 300 m, 390 m, and 450 m, reflecting topographic artifacts (blue line). However, these are absent from the Indus basin (green line).

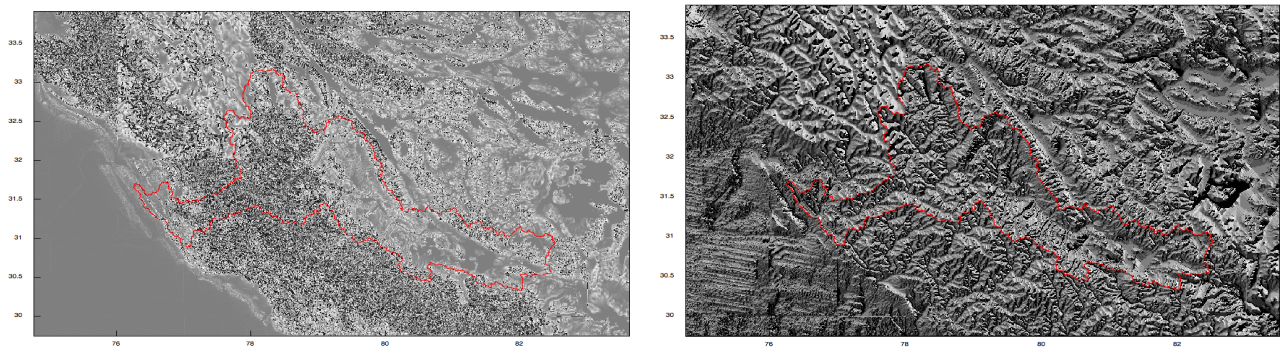

D∞ flow slopes D∞ flow angles

Figure 19: Flow slopes and angles from TauDEM for the D∞ method.

One issue of interest in predicting future floods is whether synchronization of the peak in yearly precipitation and peak in seasonal melt will coincide, and thereby produce larger floods. Mirza (2003) has identified the significant consequences of peak synchronization on floods in Bangladesh, and Barnett et al. (2005) notes that the seasonal peak flow has shifted by as much as 30 days in some areas.

Figure 23 shows both past (on the left and overlapping) and future (on the right) day-to-day correlation between temperature (which is assumed to match the melt cycle) and precipitation. The correlation varies considerably, from .15 to .3 in the observed data. In the overlap between predicted and observed data, the two correlation signals match up initially, and then quickly diverge. This may reflect inaccurate predictions which poorly reflect the trend of synchronization that has been occurring through the early 2000s.

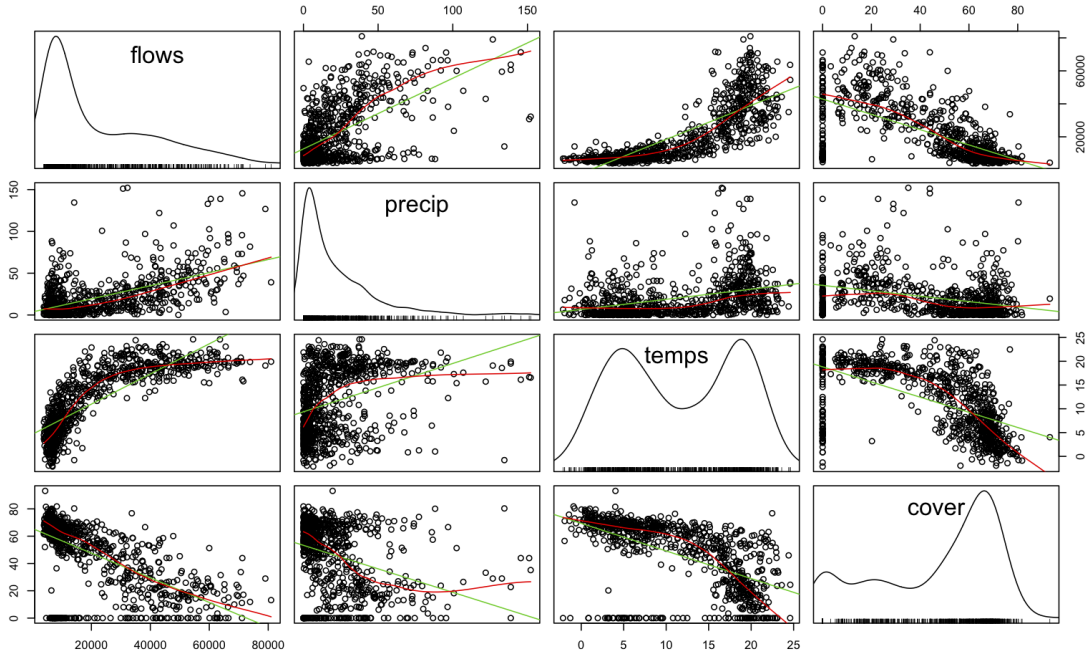

Figure 20: Scatter plot matrix for daily Bhakra dam inflows and basin averages of precipitation, temperature, and snow/ice cover. The diagonal graphs show density plots. The off-diagonal graphs show each day as a point, using the column variable on the x-axis and the row variable on the y-axis.

Appendix E. Isolating Variability

This section constructs an analytical framework for isolating the effects of temperature variability, and estimates that effect for the Bhakra basin. The goal of the analytic model is to capture the approximate stochastic relationships involved in flooding. By describing the distinct roles of melt and precipitation on flooding, it can support a model of flood probabilities changing in time.

Recently flood frequency analysis has experienced a proliferation of statistical models (Kidson and Richards, 2005). The analysis below attempts to make minimal assumptions that capture the distinct effects of precipitation and melt.

Probability models were estimated separately for precipitation and melt (with weekly temperature variation), by maximum likelihood. We use a Gaussian model for temperature and a model of precipitation with an exponential tail, allowing us to combine the distributions analytically.

The estimate of melt's contribution to flooding can be decomposed into a seasonal mean streamflow and temperature-induced variability. For the melt portion of the streamflow, let this process have a mean μ and a variance relative to the recent streamflows, σ^2. In conjunction with this, let precipitation runoff have a probability density function, $p \sim Exp(\rho)$ for $p > p_0$, or more explicitly, $f_p(p) = \alpha\delta(p) + \frac{(1-\alpha)}{\rho} e^{-(p-p_0)/\rho} u(p-p_0)$ (see figure 24). This

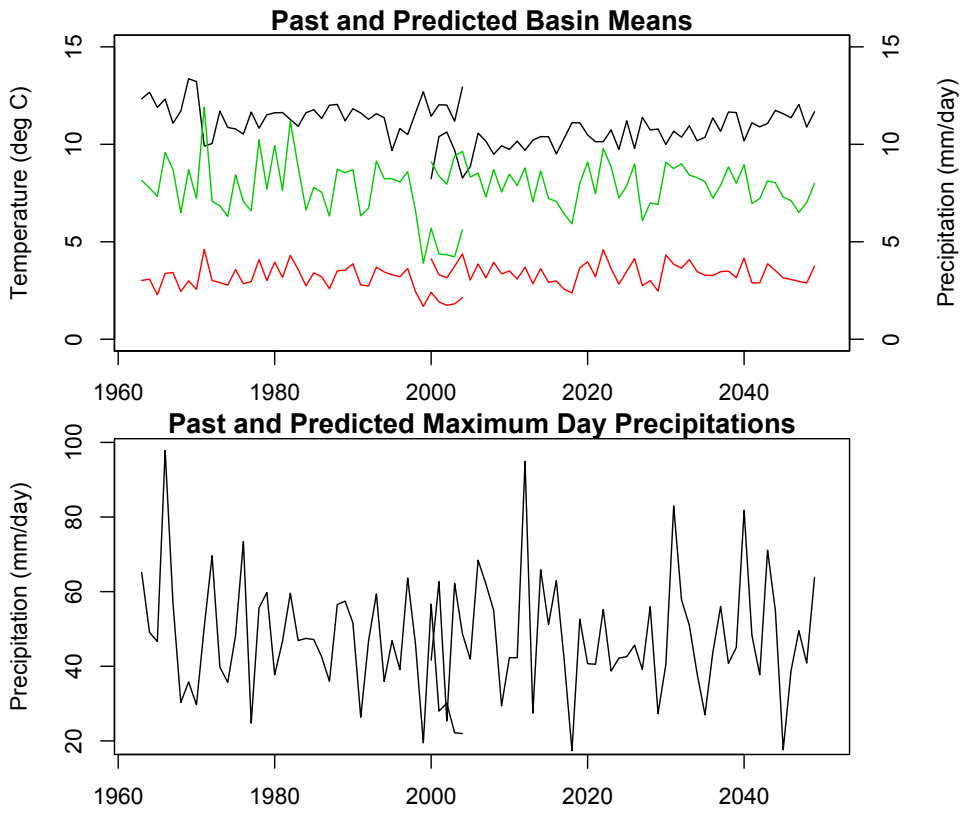

Figure 21: Past and predicted weather, averaged over the Bhakra Dam basin. In the top figure, the top curve (black) is basin-averaged temperature, showing a trend in the predicted data. The bottom curve (red) is median precipitation and middle curve (green) is the mean of daily precipitation that exceed the median precipitation. The lower figure shows maximum yearly day precipitation. Neither of these precipitation curves show trends. The discontinuity reflects the different resolutions of the historical and predicted weather maps, such that predicted temperature and precipitation includes portions of grid cells representing large regions.

reflects that the actual probability distribution may be complicated, but below a certain sustained precipitation, p_0, the precipitation is irrelevant to flooding, and above that level, precipitation events follow an approximately exponential distribution.

The sum of rainfall and melt over the entire basin, multiplied by their respective runoff coefficients as reflected in the probability distributions, is approximately equal to the stream flow. We can calculate the size of the hundred year flood from by solving for q in $P(Q \geq q) = .01$. If streamflow due to melt is constant at μ, then the size of a 100-year flood is given by,

$$\begin{aligned} P(\bar{Q} \geq q) &= \int_q^\infty \frac{(1-\alpha)}{\rho} e^{-\frac{p'-p_0-\mu}{\rho}} dp' = .01 \\ \implies q &= p_0 + \mu - \rho ln(\frac{.01}{1-\alpha}) \end{aligned}$$

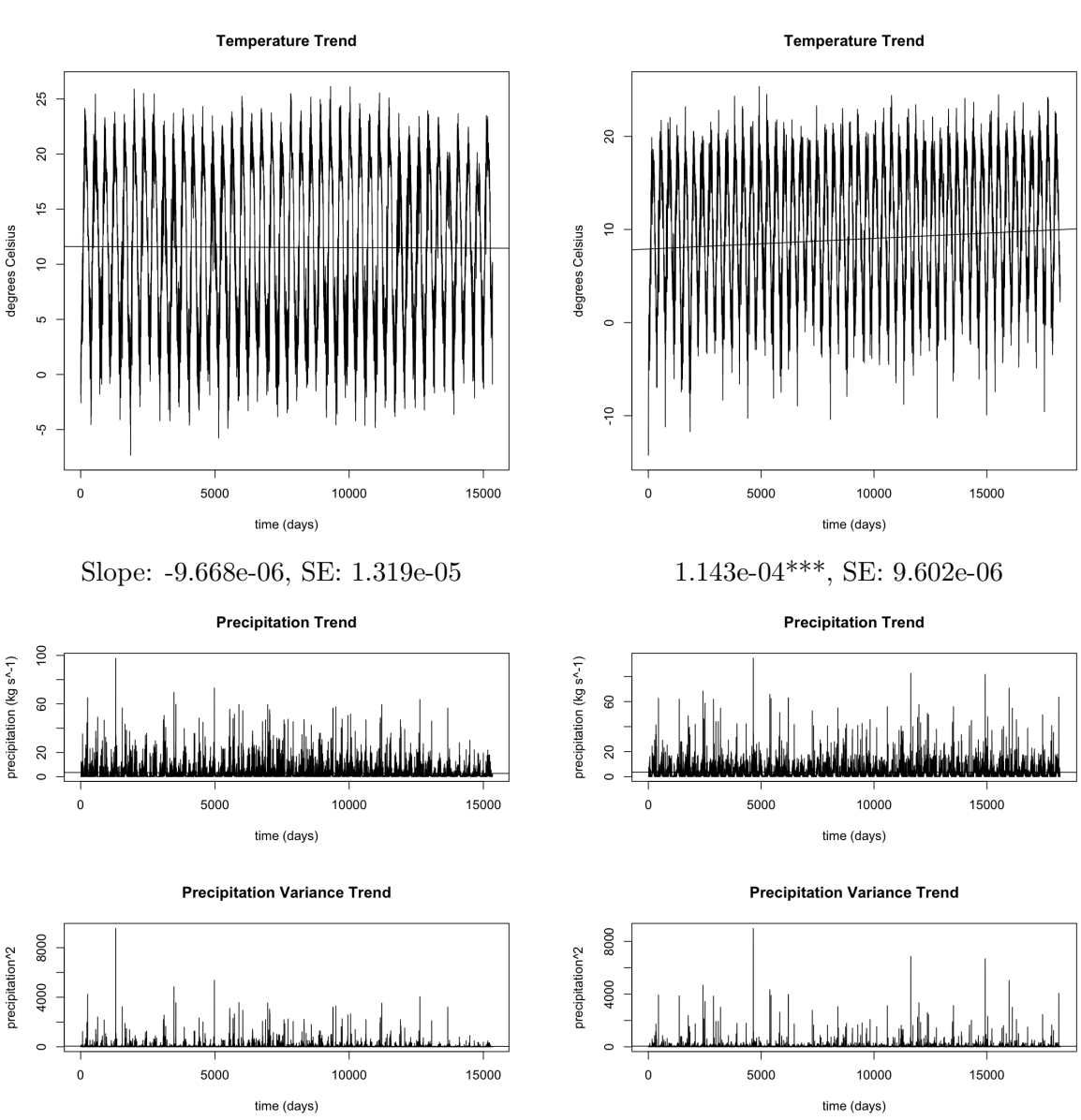

Figure 22: Changes in temperature, precipitation, and precipitation variability in the past and future. Each slope was estimated using OLS: $y_t = \beta_0 + \beta_1 t + \epsilon_t$, for different variables as y_t. Values with *** are significant at the .1% level; other values are not significant at the 10% level.

However, if streamflow due to melt is a normal distribution with mean μ and variance σ^2, the distribution of flood sizes is different and the size of a 100-year flood is given by,

$$\begin{aligned} P(\tilde{Q} \geq q) &= \int_q^\infty \frac{(1-\alpha)}{\rho} e^{-\frac{p'-p_0}{\rho}} \star n(\mu, \sigma^2) dp' \\ &= \int_q^\infty \int_{-\infty}^\infty \frac{1-\alpha}{\rho} e^{-\frac{p'-p''-p_0}{\rho}} \frac{1}{\sqrt{2\pi\sigma^2}} e^{-\frac{(p''-\mu)^2}{2\sigma^2}} dp'' dp' \\ &= \int_q^\infty \frac{1-\alpha}{\rho} e^{-\frac{p'-p_0-\mu}{\rho} + \frac{\sigma^2}{2\rho^2}} dp' \\ &= (1-\alpha) e^{-\frac{q-p_0-\mu}{\rho} + \frac{\sigma^2}{2\rho^2}} = .01 \end{aligned}$$

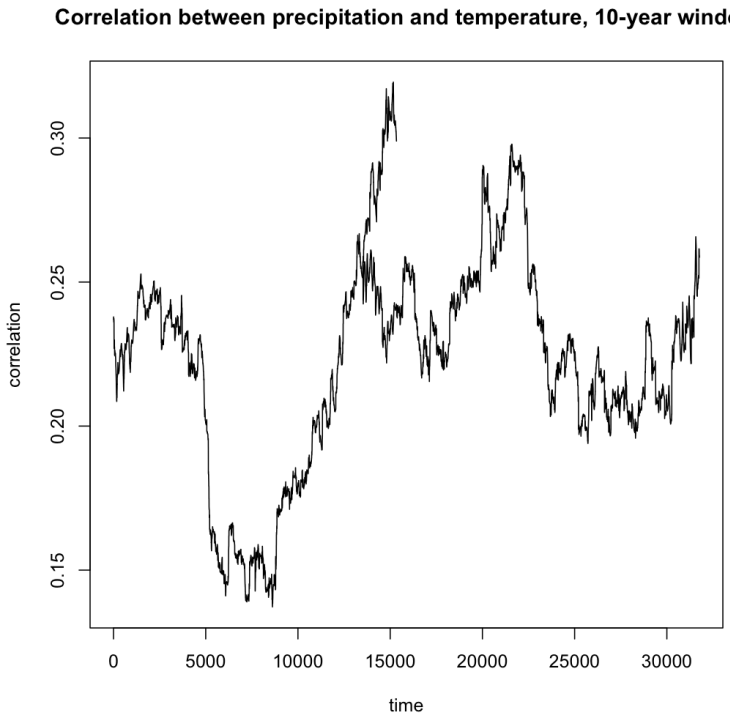

Figure 23: Correlation between precipitation and temperature, for identifying any trends toward a concurrence of the two contributions to future floods.

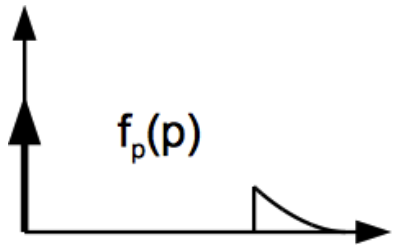

Figure 24: *Precipitation Probability Function:* $f_p(p)$ has most of its probability at $p = 0$, with the remainder as a decaying exponential starting at $p = p_0$.

For a range of parameters, this represents a significant increase in the size of the 100-year flood. See figure 25 for some numerical results.

Note that this model does not account for GLOFs or cyclonic storms, which significantly affect the weather of parts of tropical Asia and have increased over the last half century (Farooqi et al., 2005).

In the precipitation model above, the δ-function is taken to capture all of the precipitation below a given level, p_0. As a result, a maximum likelihood estimate for the model parameters fails by producing a degenerate solution with a high value of p_0. The problem with MLE in this case is that it does not capture how well the data "fits" an exponential, just how

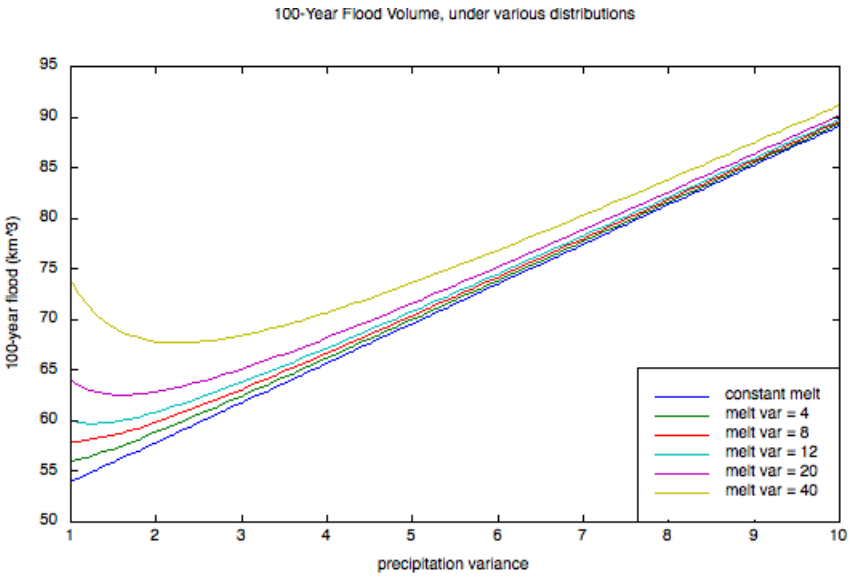

Figure 25: *100-Year Flood Volumes:* The graph shows expected 100-year volumes, given various variances in the precipitation and temperature melt, according to the model in the paper.

likely each data point is, independently. Instead, an approach using moments is used. The exponential decay rate, ρ, for a given p_0 is given by

$$\rho = \frac{\sum_{p_i \geq p_0} (p_i - p_0)}{n}$$

where n is the number of points $\geq p_0$ (this is both the MLE and method of moments result), and then the fitted p_0 is determined by the second moment,

$$\rho_0^* = \arg\min_{\rho_0} |Var(P_i) - \rho^2|$$

We fit this precipitation model to the precipitation observed over the Bhakra basin, summing all precipitation where the temperature is greater than 0°C. The result is $p_0 = 60714$, $\rho = 29720$, and $\alpha = 0.2241$.

To determine the relationship between melt and temperature, we consider the area-weighted sum of temperature in Celsius over the basin, and use OLS and an L1-Norm to estimate the coefficient on temperature for explaining streamflow. That is,

$$Q_t = \beta_1 \sum_i P_{it} \mathbf{1}\{T_{it} > 0\} + \beta_2 \sum_i T_{it} \mathbf{S_{it}} > \mathbf{0} + \epsilon_t$$

Where Q_t is the streamflow on a given day, P_{it} is the precipitation in region i, and T_{it} is the temperature in region i, and S_{it} is the snowcover in region i. This produces a simple temperature coefficient melt model. The estimate is shown below.

The melt model is then estimated based on the mean melt and the variability of melt relative to the mean of the surrounding 30 days. The result is $\mu = 1.2447$ and $\sigma^2 = 52182000$.

	OLS	L1-Norm
Melt	12447.18***	11424.05***
	(128.88)	(151.26)
Rainfall	3330.56***	4089.42***
	(105.65)	(238.13)
R^2	0.80	
Adj. R^2	0.80	
Num. obs.	4970	5600
Percentile		0.50

$^{***}p < 0.01$, $^{**}p < 0.05$, $^{*}p < 0.1$

OLS	Mean Portion	Variance Portion
Melt	68.7%	59.8%
Rainfall	14.1%	10.3%
L1-Norm	Mean Portion	Variance Portion
Melt	63.3%	33.1%
Rainfall	15.7%	11.7%

Figure 26: The top shows the coefficient estimates for melt and rainfall. The values in the estimate are normalized by the mean melt and rainfall, so these values can be understood in relation to each other. As a result of these models, the portion of the streamflow explained by melt and the variance in the streamflow explained by melt are given in the second table. These values are close to the 59% given in (Singh and Jain, 2002).

The models and corresponding binned data are shown in figure 27.

Based on this simple model, at the Bhakra dam, the 10-year single-day flood is 91.7% attributable to precipitation (the remaining comes from melt). The 100-year single-day flood is 94.6% from precipitation. An estimate of the size of a 10-year flood that adds the role of variability in melt is only 1% higher.

	10-Year	Increase	100-Year	Increase
Precipitation-only	88854 ft^3/s	0%	150400 ft^3/s	0%
Precipitation and Average Melt	101300 ft^3/s	14.01%	162850 ft^3/s	8.28%
Precipitation and Variable Melt	102280 ft^3/s	15.11%	163820 ft^3/s	8.93%

Appendix F. Supplement 7: Impacts

The climate change profiles for this region predict significant increases in annual temperatures, total precipitation, and the prevalence of extremely warm and wet seasons. All of these will contribute to flood risk, through greater precipitation runoff and melt runoff. In particular, temperatures are likely to increase in most areas, but the effect on precipitation shows a less clear trend, and studies of actual precipitation trends are inconsistent across southern Asia (Cruz et al., 2007). Extreme weather events are also expected to increase, both through heavy rainfall and hot ($> 30°$C) days, which will increase the propensity for disasters. Finally, greater winter accumulation is predicted in some regions (Dyurgerov et al., 2005), which combined with a sharp seasonal temperature transitions may result in significant additional runoff in the seasonal floods and increases in the variability of runoff. However, the complexity of mountain topography makes modeling the effects of climate change unreliable for much of this area (Solomon et al., 2007, Box 11.3: Climatic Change in Mountain Regions).

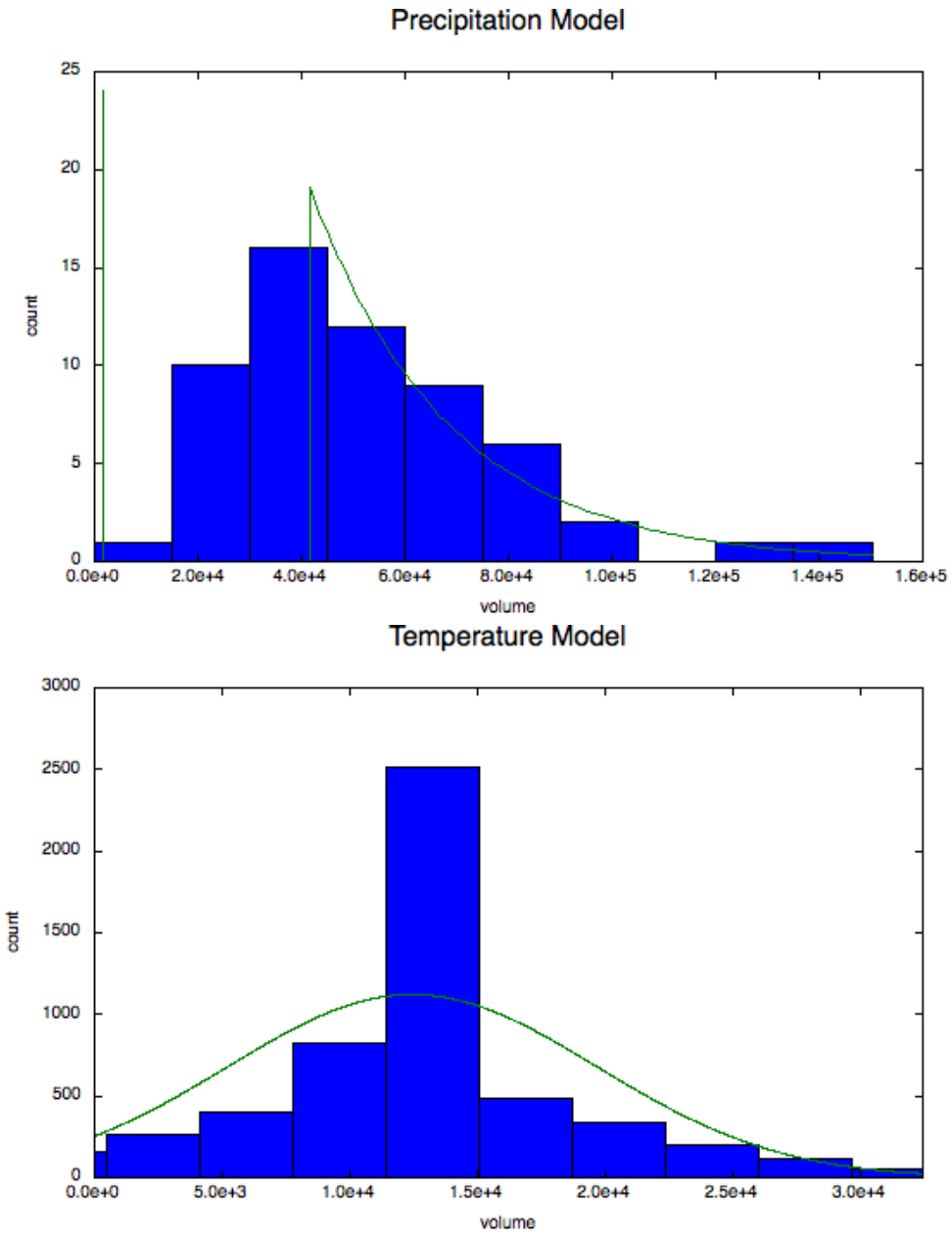

Figure 27: Precipitation and melt model.

Pakistan has been subject to progressively increasing flood risk in recent decades (see figure 28), culminating in the recent 2010 flood, which affected 20 million people (Cross, 2010). While this observed effect is partly due to better reporting, and significantly driven by increased populations in vulnerable areas, natural drivers, such as increases in precipitation and melt and decreases in glacial buffering, may also be responsible. These events reverberate throughout an economy, and identifying how their likely magnitude and frequency will change as glaciers melt will help governments plan their infrastructure development.

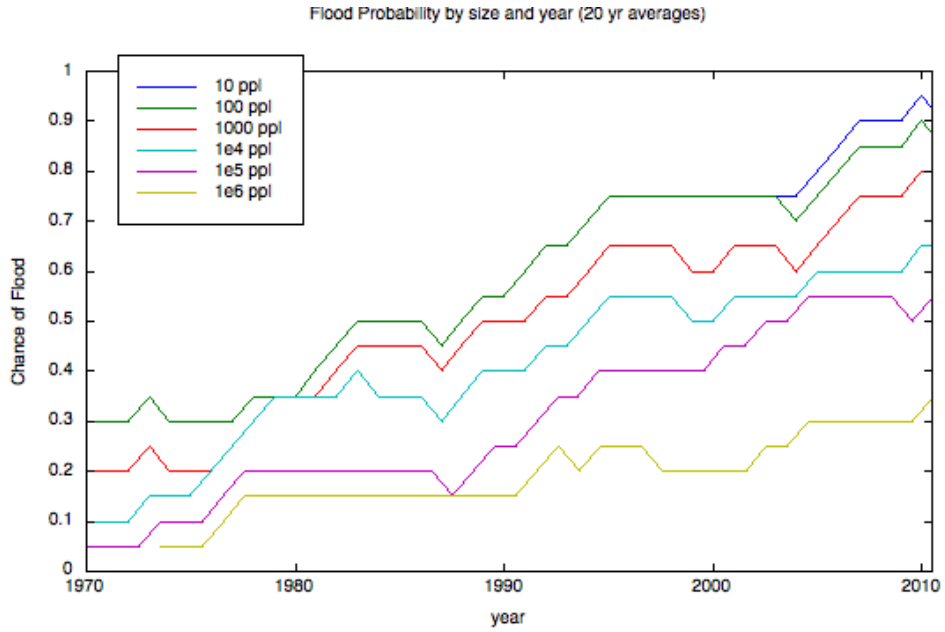

Figure 28: *Chance of Flooding in Pakistan:* Probability of floods impacting at least a given population in each year, as running 20-year averages. Source: CRED EM-DAT database.

References

Ageta, Y. (1983). Characteristics of mass balance of the summer-accumulation type glacier in the Nepal Himalaya-I. *Seppyo*, 45(2):81–105.

Ahern, M., Kovats, R., Wilkinson, P., Few, R., and Matthies, F. (2005). Global health impacts of floods: epidemiologic evidence. *Epidemiologic Reviews*, 27(1):36.

Barnett, T., Adam, J., and Lettenmaier, D. (2005). Potential impacts of a warming climate on water availability in snow-dominated regions. *Nature*, 438(7066):303–309.

Becker, A. and Bugmann, H. (1997). Predicting global change impacts on mountain hydrology and ecology: integrated catchment hydrology/altitudinal gradient studies: workshop report: documentation resulting from an international workshop, kathmandu, nepal, 30 march 1996. *Global Change Report*.

Cenderelli, D. and Wohl, E. (2001). Peak discharge estimates of glacial-lake outburst floods and "normal" climatic floods in the Mount Everest region, Nepal. *Geomorphology*, 40(1-2):57–90.

Cross, S. R. (2010). Pakistan Floods: The Deluge of Disaster - Facts & Figures as of 15 September 2010. `http://www.reliefweb.int/rw/rwb.nsf/db900SID/LSGZ-89GD7W?OpenDocument`, retrieved December 4, 2010.

Cruz, R., Harasawa, H., Lal, M., Wu, S., Anokhin, Y., Punsalmaa, B., Honda, Y., Jafari, M., Li, C., and Ninh, N. H. (2007). Asia.

Dairaku, K., Emori, S., and Nozawa, T. (2008). Impacts of global warming on hydrological cycles in the Asian monsoon region. *Advances in Atmospheric Sciences*, 25(6):960–973.

Desloges, J. and Church, M. (1992). Geomorphic implications of glacier outburst flooding: Noeick River valley, British Columbia. *Canadian Journal of Earth Sciences*, 29(3):551–564.

Dyurgerov, M., Meier, M., University of Colorado, B. I. o. A., and Research, A. (2005). *Glaciers and the changing Earth system: a 2004 snapshot*. Institute of Arctic and Alpine Research, University of Colorado Boulder.

Farooqi, A., Khan, A., and Mir, H. (2005). Climate change perspective in Pakistan. *Pakistan Journal of Meteorology Vol*, 2(3).

Fujita, K. (2008). Effect of precipitation seasonality on climatic sensitivity of glacier mass balance. *Earth and Planetary Science Letters*, 276(1):14–19.

Grody, N. C. and Basist, A. N. (1996). Global identification of snowcover using ssm/i measurements. *Geoscience and Remote Sensing, IEEE Transactions on*, 34(1):237–249.

Huang, M. (1990). On the temperature distribution of glaciers in China. *Journal of Glaciology*, 36(123):210–215.

Jeelani, G., Feddema, J., van der Veen, C., and Stearns, L. (2012). Role of snow and glacier melt in controlling river hydrology in liddar watershed (western himalaya) under current and future climate. *Water Resources Research*, 48(12):W12508.

Kaser, G., Juen, I., Georges, C., Gómez, J., and Tamayo, W. (2003). The impact of glaciers on the runoff and the reconstruction of mass balance history from hydrological data in the tropical Cordillera Blanca, Peru. *Journal of Hydrology*, 282(1-4):130–144.

Kattelmann, R. (2003). Glacial Lake Outburst Floods in the Nepal Himalaya: A Manageable Hazard? *Natural Hazards*, 28(1):145–154.

Kayastha, R., Ageta, Y., Nakawo, M., Fujita, K., Sakai, A., and Matsuda, Y. (2003). Positive degree-day factors for ice ablation on four glaciers in the Nepalese Himalayas and Qinghai-Tibetan Plateau. *Bulletin of glaciological research*, 20:7–14.

Kidson, R. and Richards, K. (2005). Flood frequency analysis: assumptions and alternatives. *Progress in Physical Geography*, 29(3):392.

Kundzewicz, Z. and Takeuchi, K. (1999). Flood protection and management: quo vadimus?/Protection et aménagement contre les inondations: quo vadimus? *Hydrological Sciences Journal*, 44(3):417–432.

Menke, W. (2012). *Geophysical data analysis: Discrete inverse theory*. Academic press.

Mirza, M., Warrick, R., and Ericksen, N. (2003). The implications of climate change on floods of the Ganges, Brahmaputra and Meghna rivers in Bangladesh. *Climatic Change*, 57(3):287–318.

Mirza, M. M. Q. (2003). Three recent extreme floods in bangladesh: a hydro-meteorological analysis. In *Flood Problem and Management in South Asia*, pages 35–64. Springer.

Ohmura, A. (2001). Physical basis for the temperature-based melt-index method. *Journal of Applied Meteorology*, 40(4):753–761.

Pal, I., Lall, U., Robertson, A., Cane, M., and Bansal, R. (2012a). Predictability of western himalayan river flow: melt seasonal inflow into bhakra reservoir in northern india. *Hydrol. Earth Syst. Sci. Discuss*, 9:8137–8172.

Pal, I., Lall, U., Robertson, A. W., Cane, M. A., and Bansal, R. (2012b). Diagnostics of western himalayan satluj river flow: Warm season (mam/jjas) inflow into bhakra dam in india. *Journal of Hydrology*.

Parry, M. (2007). *Climate Change 2007: impacts, adaptation and vulnerability: contribution of Working Group II to the fourth assessment report of the Intergovernmental Panel on Climate Change*. Cambridge Univ Pr.

Richardson, S. and Reynolds, J. (2000). An overview of glacial hazards in the Himalayas. *Quaternary International*, 65:31–47.

Singh, P. and Bengtsson, L. (2004). Hydrological sensitivity of a large himalayan basin to climate change. *Hydrological Processes*, 18(13):2363–2385.

Singh, P. and Bengtsson, L. (2005). Impact of warmer climate on melt and evaporation for the rainfed, snowfed and glacierfed basins in the Himalayan region. *Journal of Hydrology*, 300(1-4):140–154.

Singh, P. and Jain, S. (2002). Snow and glacier melt in the satluj river at bhakra dam in the western himalayan region. *Hydrological sciences journal*, 47(1):93–106.

Singh, P. and Jain, S. (2003). Modelling of streamflow and its components for a large himalayan basin with predominant snowmelt yields. *Hydrological sciences journal*, 48(2):257–276.

Singh, P., Kumar, N., and Arora, M. (2000). Degree–day factors for snow and ice for dokriani glacier, garhwal himalayas. *Journal of Hydrology*, 235(1):1–11.

Solomon, S. et al. (2007). *Climate change 2007: the physical science basis*. Cambridge University Press Cambridge.

Tarboton, D. G. (2005). Terrain analysis using digital elevation models (taudem). *Utah Water*.

Te Chow, V. (1959). *Open channel hydraulics*. McGraw-Hill Book Company, Inc; New York.

Wescoat Jr, J. (1991). Managing the Indus River basin in light of climate change:: Four conceptual approaches. *Global Environmental Change*, 1(5):381–395.

Xu, J., Grumbine, R. E., Shrestha, A., Eriksson, M., Yang, X., Wang, Y., and Wilkes, A. (2009). The melting himalayas: cascading effects of climate change on water, biodiversity, and livelihoods. *Conservation Biology*, 23(3):520–530.